The Thesis Committee for Daniel Jeffrey Groom
Certifies that this is the approved version of the following thesis:

The Effect of Nanocatalyst Size on Performance and Degradation in the Cathode of Proton Exchange Membrane Fuel Cells

APPROVED BY
SUPERVISING COMMITTEE:

Supervisor: _____
Paulo Ferreira

_____
Llewellyn K. Rabenberg

The Effect of Nanocatalyst Size on Performance and Degradation in the Cathode of Proton Exchange Membrane Fuel Cells

by

Daniel Jeffrey Groom, BSCBE

Thesis

Presented to the Faculty of the Graduate School of

The University of Texas at Austin

in Partial Fulfillment

of the Requirements

for the Degree of

Master of Science in Engineering

The University of Texas at Austin

December, 2011

Dedication

Dedicated to my family.

Acknowledgements

Most of all, I would like to thank my supervisor, Paulo Ferreira, for guidance and insight during my research on proton exchange membrane fuel cells. I would like to thank my family for supporting my decision to pursue graduate studies in engineering. Finally, I would like to thank the members of my research group for their support and help.

Abstract

The Effect of Nanocatalyst Size on Performance and Degradation in the Cathode of Proton Exchange Membrane Fuel Cells

Daniel Jeffrey Groom, MSE

The University of Texas at Austin, 2011

Supervisor: Paulo Ferreira

This thesis discusses the role of initial particle size on the mechanisms of surface area loss of carbon-supported platinum (Pt) electrocatalysts in the cathode of proton exchange membrane fuel cells. Electrocatalyst decay protocols were used to accelerate cathode performance loss for Pt catalysts. Four cathodes with mean platinum particle sizes of 2.1, 3.5, 6.7 and 11.3 nm were evaluated to elucidate the impact of particle size on initial performance and subsequent degradation, when subjected to identical potential cycles. The degradation of Pt electrochemically active surface area (ECA) was significantly greater for 2.1 and 3.5 nm initial sizes compared to 6.7 and 11.3 nm initial sizes. As expected, the ECA loss of the cathodes shows an inverse proportionality with initial particle size. However, the initial performance of the 11.3 nm initial particle size electrode was significantly lower than the three smaller sizes. Thus, an initial Pt particle size of 6.7 nm was identified to offer the ideal balance performance and durability. The current state of standardization in characterizing particle size by transmission electron

microscopy (TEM) is also investigated. The result is a standardized protocol for image acquisition and analysis.

Table of Contents

List of Figures

Chapter 1: Introduction

1.1 Motivation

There are more than 500 million internal combustion engine based vehicles world-wide [1], and vehicular pollution contributes approximately 1 billion tones of CO_2 green house gases [2] every year. The research community predicts approximately 1 billion vehicles world-wide by the year 2025, which poses a significant pollution challenge if left un-addressed. Therefore, there is an intense drive to switch to less polluting energy conversion devices for transportation applications. Generating electricity through the electrochemical conversion of hydrogen and oxygen to water, Proton Exchange Membrane Fuel Cells (PEMFCs) offer the ability to reduce the world's reliance on rapidly depleting fossil fuels and decrease the production of greenhouse gases. PEMFCs are of particular interest because of their high energy density (approximately 0.7-0.9 W/cm^2) [3], low operating temperatures (approximately 80 °C), and clean well-to-wheel carbon footprint [4]. Due to their attractive attributes, several studies now envisage PEMFC devices for stationary and portable power applications (1-50 W) [5]. However, PEMFC technology is still in its early stages of development, and a broad array of obstacles must be overcome for PEMFCs to become a viable source of sustainable energy. In particular, PEMFCs experience severe degradation in the form of decreased lifecycle over the range of practical operating conditions [6,7]. For PEMFCs to become a viable and widespread technology, advancements must address durability while simultaneously minimizing the overall cost of the system.

Studies of PEMFC membrane electrode assemblies (MEAs) have revealed that degradation of Pt nanoparticles used as catalysts in the cathode of PEMFCs serves as the primary obstacle for meeting the durability requirements for vehicular applications,

impeding widespread deployment of this technology. The dominant cause of PEMFC degradation is loss of electrochemically active surface area (ECA) of Pt nanoparticles in the cathode [8-14]. ECA loss has in turn been shown to result from four specific degradation mechanisms namely, coalescence, Ostwald ripening, dissolution and re-precipitation and detachment from carbon support, the results of which are either coarsening or loss of Pt mass to electrochemically inaccessible regions of the cell [15]. However, the relative contribution of each degradation mechanism to ECA loss is poorly understood. For example, ECA loss has been shown to depend on operating conditions [16-18] and on the initial size of nanoparticles in the cathode [15, 19]. As a result, there is considerable interest in finding an ideal particle size and an optimal set of operating conditions to enhance durability.

Unfortunately, it is often difficult or impossible to compare results and conclusions from TEM studies of PEMFCs due to differences in their approach to characterizing particle size and shape. Sources of error vary widely between studies analyzing the effect of nanoparticle size in the cathode of PEMFCs. Without a standardized approach to image acquisition and analysis, separate researchers may analyze the same sample but arrive at vastly different particle size distributions. Even when analyzing the same set of images, separate investigators may reach different conclusions due to bias introduced by not following a standard. In short, the current state of TEM as a technique for nanometrology precludes reproducibility. Key sources of error and variability have not been yet quantitatively studied, so a standardized protocol for characterizing particle size by TEM cannot be developed from existing data.

1.2 Objectives, Main Contributions, and Approach

1.2.1 Objectives

To address the aforementioned issues, this work investigates Pt electrocatalyst degradation in the cathode of PEMFCs through TEM characterization of carbon-supported Pt nanoparticles. The objective of this work is twofold:

1. To investigate the effect of initial particle size on the mechanisms of ECA loss, initial electrochemical performance, and degradation. Four different initial sizes in the cathode are examined.
2. To develop a standard for characterizing particle size that minimizes error and variability. The topics addressed are error inherent to specific size metrics, the use of exclusion criteria, and particle overlap.

1.2.2 Main Contributions

1. This is the first study to investigate a broad range of particle sizes. In particular, this work demonstrates that the mechanisms for ECA loss exhibit an inverse proportionality with particle size. Moreover, the particle size effect is shown to play a minimal role above a minimum size, which yields insights into the dominant degradation mechanism. A minimum particle size of 5 nm is unambiguously shown to offer enhanced stability in the cathode. As a result, this work identifies an ideal particle size distribution that balances initial performance and durability among a set of four different initial sizes. These results form a framework for future work to further optimizing performance and durability over a narrower range of initial particle sizes by varying heat treatments and initial particle size distributions. The main contribution of these results demonstrates

that efforts to improve performance by decreasing the initial particle size below 5 nm will incur substantial losses to durability.

2. By quantifying the size and shape dependence of four common shape metrics, this work invalidates their use as exclusion criteria. This result is crucial for future PEMFC research because it eliminates a key source of variability, thereby ensuring reproducibility.

3. This work develops a mathematical model for overlapping particles generic to any three-dimensional shape. This model is used to develop a program that simulates TEM images of overlapping spherical particles. The application of edge detection techniques to the results of these simulations identifies root causes of overlap mischaracterization, providing a basis for a standardized approach to characterizing particle overlap.

4. By quantifying the inherent error of common size metrics, this work develops a standardized image acquisition protocol based on a novel metric, equivalent error. This protocol allows the TEM operator to select a magnification based on an initial estimate of particle size, such that the error due to pixel resolution will be below a maximum threshold. These results are applied to image acquisition for determining particle size distributions in this study, leading to an equivalent error of less than 5% for each sample. By eliminating a key source of error and variability, this result ensures reproducibility, thereby allowing for direct comparisons between the particle size distributions of each sample.

1.2.3 Approach

The Role of Initial Particle Size

The first goal of this work is to elucidate the effect of initial particle size in the cathode of PEMFCs on initial performance and degradation. This approach involves systematically varying the initial particle size in the cathodes of different PEMFCs and subjecting each sample to identical electrochemical decay protocols. To accomplish this task, this work aims to quantify the change in particle size in the cathode throughout the lifecycle of the PEMFC.

Standardized TEM Protocol for Nanometrology

The second goal of this work is a prerequisite to completing the first. Before investigating nanoparticle growth in PEMFC cathodes, it is necessary to develop a standardized approach to TEM characterization of particle size. This work investigates and quantifies three key sources of error and variability in TEM particle size studies. The first step in the approach for this task is to simulate TEM image formation for the instrument used in this study of particles with known three-dimensional sizes and shapes. Analyzing the results of these simulations with digital image processing software commonly used to determine particle size allows for the identification of sources of error ranging from image formation to image analysis.

1.3: Organization of the Thesis

The remainder of the thesis is divided into chapters that cover topics on ECA loss in PEMFCs and the standardized use of TEM for nanometrology. Focusing on the current state of understanding, Chapter 2 begins with a brief overview of the PEMFC followed

by a literature survey that describes the relevant work completed to date on PEMFC degradation. Chapter 2 continues by defining each of the identified mechanisms for ECA loss, providing an overview of the evidence for each mechanism and precisely what this study can and cannot say about each. Chapter 2 ends with a brief discussion on standardization in TEM for nanometrology. Chapter 3 details the mathematical modeling and simulations that serve as a basis for the standardized approach to characterizing particle size by TEM. Applying the results of Chapter 3, Chapter 4 contains the experimental results of TEM characterization of samples representing four different initial sizes in the cathode. Chapter 4 ends by providing the results and discussion for TEM characterization of the 12 samples considered in this work to investigate the effects of initial particle size on PEMFC performance. The thesis ends with Chapter 5, which discusses the conclusions reached from Chapters 3-4.

Chapter 2: State of Understanding

2.1 Durability of PEMFCs

Catalyst morphology changes in PEMFCs were first reported by Wilson et al., who demonstrated a direct correlation between catalyst degradation and lower electrochemical performance [20]. Thereafter, Darling et al. developed models to describe platinum dissolution, and proposed that platinum is stable at lower and higher voltages but unstable during transition from a lower to higher voltage during cycling [21]. Platinum nanocatalyst movement through anode-gas diffusion media, anode, membrane, cathode, and cathode-gas diffusion media has also been modeled where the role of an oxide layer on platinum during cycling is discussed [22]. Xie et al. performed detailed electron microscopy analysis of Pt and Pt-alloy (Pt_3Cr and Pt_2CoCr) catalysts loaded on the MEAs and demonstrated that potential cycling accelerated catalyst changes, and influenced carbon support [23, 24]. In a different body of work, Borup et al. demonstrated that catalyst and catalyst support degradation accelerated at higher potentials, higher operating temperatures, and lower relative humidity [25]. Akita et al. performed analytical electron microscopy studies on cycled MEAs loaded with Pt-alloy and Pt nanocatalysts and showed the presence of dendritic particles [16]. Akita et al. proposed that hydrogen permeation from the anode reduced the platinum ions, diffusing into the membrane from the cathode, into platinum particles; these particles attained non-equilibrium shapes closer to the cathode where the hydrogen concentration was lower, but formed equilibrium shapes closer to the anode where hydrogen concentration was higher [16]. In a more detailed group of papers following TEM analysis procedures established in the literature [26], Ferreira et al. [27, 28] and Shao-Horn et al. [15]

reported on the influence of potential cycling on the morphology of approximately 2 nm initial size nanocatalysts loaded in the cathode of MEAs, and proposed the following phenomenological models for several particle growth mechanisms that become active during PEMFC cycling operations: (i) nanoscale 2D Ostwald ripening, (ii) particle migration and coalescence, (iii) detachment from carbon support, and (iv) platinum dissolution and re-precipitation inside the ionomer membrane. Other research groups have reported platinum nanoparticles in the membrane [29]. More recently, Holby et al. modeled changes in nanocatalyst particle size distribution upon cycling, and concluded that approximately 4-5 nm initial nanoparticle size loading was optimal for PEMFC durability during cycling, due to the lowering of Gibbs-Thomson energy for dissolution [30]. Studying this same range of initial sizes, Hartl et al. combined transmission electron microscopy technique with accelerated stress tests to clearly demonstrate local changes in catalyst morphology before and after potential cycling [31].

The heart of a PEMFC system is a Membrane Electrode Assembly (MEA) comprising of a proton conducting polymer membrane ($\sigma_{proton} > 0.1$ S cm^{-1}), and electrodes (cathode and anode) that sandwich this membrane from either side, as illustrated in Figure 2.1. Interconnects and gas diffusion layers, which supply fuel and remove by-products, cover the electrodes and complete this assembly. The anode side of the MEA assembly is fed with hydrogen, while air or oxygen is supplied to the cathode side. Hydrogen is oxidized at the anode (Hydrogen Oxidation Reaction (HOR): $H_2 \rightarrow 2H^+ + 2e^-$) and converted to protons thereby releasing electrons. The electrons complete the circuit by entering the cathode and reducing the incoming air/oxygen fuel to oxide ions (Oxygen Reduction Reaction (ORR): $O_2 + 4H^+ + 4e^- \rightarrow 2H_2O$). Protons from the anode traverse through the membrane and produce water as a by-product in the cathode, which is removed by adequate water management techniques. The voltage difference of

E_o = 1.195 V for the complete reaction: $H_2 + ½ O_2 \rightarrow H_2O$ provides useful work for several applications. Typically, the reactions are inefficient and the HOR and ORR kinetics are sluggish. Thus, MEA electrodes comprise of carbon supported Pt nanocatalysts, which owing to their high surface-to-volume ratio and chemical inertness, make available more reaction sites for catalytic activity and enhance the abovementioned kinetic reactions. The advent of various dispersion technologies has lowered Pt nanocatalyst loading on electrodes to approximately ≤ 0.2 mg/cm^2. This translates to approximately 24 gPt for a 85kW fuel cell stack in a 75 kWnet automotive fuel cell system, thereby increasing the cost-competitiveness of PEMFCs relative to other forms of energy conversion devices and systems. Despite these technological advances, PEMFCs still face significant technological challenges before they become practically viable; one of the most critical is their durability during potential cycling that falls short of the 5,000 and 40,000 hours operation objective set by the United States Department of Energy for vehicular and stationary applications, respectively. Several studies in the past have related morphological changes in the nanocatalysts loaded at the cathode side, during fuel cell operation with the observed performance degradation. These studies have determined that the dominant cause of PEMFC degradation is loss of electrochemically active surface area (ECA) of Pt nanoparticles in the cathode.

Several experimental and modeling studies concerning other aspects of MEA durability such as catalyst particles inside the membrane [29], degradation of membranes due to the presence of catalyst particles [32, 33], influence of cycling on carbon support [34-36], as well as development of new carbon support materials [5], have also been reported.

The role of initial particle size has emerged as a key topic in balancing performance and durability. Although ECA loss and growth has been shown to have an

inverse proportionality with initial particle size, the possible benefit of optimizing particle size has been a subject of debate in the literature. Shao-Horn et al. provided evidence for a particle size effect on ECA loss and growth in aqueous solution for particles subjected to high temperature heat treatments [15]. Studying particles with different initial loadings but identical heat treatments through in-situ small angle X-ray scattering, Smith et al. provided additional evidence for a particle size effect on ECA loss and growth [19]. In a study varying initial particle size, dispersion of particles on the carbon support, and heat treatment, Makharia et al. also find that ECA loss is inversely proportional with initial particle size [37]. In addition, their study finds evidence that heat treatment protocols in the initial ripening process may also inhibit ECA loss, providing possible evidence for an unknown heat treatment effect [37]. Due to the small range of sizes considered and the sources of variability within and between these studies, such as heat treatment protocols, initial loadings, and initial PSDs, it is unclear whether or not it is possible to optimize performance and stability by selecting an ideal initial particle size.

Previous studies have focused on only a limited set of initial particle sizes ranging from 2-5 nm, with each study reaching the conclusion that increasing particle size above this range will lead to enhanced durability while incurring a tradeoff with initial performance. It is unclear, however, how much particle size will have to increase above the conventional 2-3 nm range to substantially improve durability and how much initial performance loss this will incur. Shao-Horn et al. propose that only a modest increase above the 2-3 nm range may be necessary [15]. The work of Holby et al. further explores larger sizes, arriving at an ideal initial size of 4-5 nm [30]. Both Shao-Horn et al. and Holby et al. attribute ECA loss of initial sizes below 5 nm to increasing Pt dissolution rates with decreasing particle size [15, 30]. In a study of 2, 3, 4, and 5 nm initial mean particle sizes, Hartl et al. demonstrate that initial sizes of 4-5 nm offer the most stability,

concluding that initial sizes will need to be above the 4-5 nm range to offer acceptable stability [31]. Hartl et al. explain their results for 2-5 nm initial sizes by providing a detailed theoretical treatment that attributes ECA loss of sizes below 5 nm to Pt dissolution. The theoretical treatment of Hartl et al. shows that Pt dissolution rates increase with decreasing particle size in the range of 2-5 nm. However, the modeling presented by Hartl et al. also demonstrates an unexpected step-wise decrease in Pt dissolution rates when particle sizes increases above 5 nm, from which it is extrapolated that sizes only slightly above 5 nm will offer substantial improvements in durability. While the experimental results and theoretical treatment from these studies demonstrates that ECA loss due to a dominant Pt dissolution mechanism shows an inverse proportionality with initial sizes between 2-5 nm, there is no experimental evidence that compares sizes above and below this range. Thus, there is no unique experimental evidence that sizes greater than 4-5 nm offer substantially enhanced stability.

To address these issues, this work aims to elucidate the effect of particle size in the cathode of the PEMFC by systematically varying the initial particle size in the cathodes of different PEMFCs and subjecting each sample to identical electrochemical decay protocols. Initial particle sizes above and below 5 nm are investigated. To accomplish this task, this work aims to quantify the change in particle size in the cathode throughout the lifecycle of the PEMFC, from catalyst and MEA fabrication to the end of life state after potential cycling.

2.2 Mechanisms of ECA Loss

ECA is defined as Pt surface area that contributes electrochemically to the ORR divided by Pt mass, such that ECA has units of m^2/g_{Pt}. Pt mass may contribute

electrochemically to the ORR only if it is in contact with the carbon support, which serves as the electrically conducting phase of the cathode. Moreover, dimensional analysis reveals that ECA has an inverse proportionality with particle size. For example, in the simplest case of a sphere with diameter d, the ratio of surface area to mass yields a scalar multiplied by $1/d$. Thus, the mechanisms of ECA loss fall into two broad categories, the first involving coarsening of carbon-supported Pt nanoparticles and the second involving loss of Pt mass from the carbon support such that electrochemical activity is lost. Coarsening of Pt nanoparticles on the carbon support, in turn, is described by a combination of two growth mechanisms, namely migration/coalescence and Ostwald ripening. Similarly, loss of Pt from the carbon support results from a combination of two mechanisms, namely detachment of nanoparticles from the carbon support and Pt dissolution. There are numerous sources of variation in the relative contributions to ECA loss of the mechanisms from each category, such as operating conditions, initial particle size, loading, heat treatment, and surface area and graphitization of the carbon support. The sections below define each of these four mechanisms, which are illustrated in Figure 2.2 [15].

Detachment of Catalyst Particles from the Carbon Support

As shown in Figure 2.2a, catalyst particle detachment results in ECA loss because Pt particles must have contact with electrically conducting carbon to catalyze the ORR. The primary cause of particle detachment is corrosion of the carbon support. With a standard potential of 0.207V v. RHE, carbon corrosion is thermodynamically favorable in the cathode, where the potential is 1.195V v. RHE at open circuit and standard temperature and pressure. In the temperature regime of approximately 80°C for low-

temperature PEMFCs, however, carbon corrosion kinetics are negligible at cell potentials below 0.8V v. RHE when compared to the lifecycle of the cell [37]. The kinetics of carbon corrosion in PEMFCs are more rapid at cell potentials above 1.1V v. RHE, above which significant loss of carbon mass has been reported [37]. SEM studies demonstrate that accelerated carbon corrosion occurs in the region between Pt particles and the carbon support, prompting a debate that Pt-carbon interactions may influence the corrosion rate [38]. ECA loss has been reported to decrease as the degree of graphitization of the carbon increases, although these findings were not decoupled from a possible particle size effect [6]. Variations in ECA loss due to carbon corrosion with operating conditions such as temperature and relative humidity have also been reported [17].

Pt Dissolution

Direct evidence for Pt dissolution in the cathode of PEMFCs comes from the detection of soluble Pt species in the membrane of electrochemically aged MEAs and in water separated from the cathode effluent [13, 29]. Theoretical and experimental reports of Pt dissolution in PEMFCs indicate that the kinetics of Pt dissolution are negligible compared to the lifecycle of the cell at potentials below 0.7V v. RHE and significant to ECA loss at potentials above 0.8V v. RHE [15]. As a result, it has been reported that the mass percentage of Pt in the cathode decreases more rapidly with increasing voltage. Moreover, high potential and high temperature operations have been reported to accelerate Pt dissolution rates [6, 15]. Increasing Pt dissolution rates with decreasing particle size have been reported as well, attributed to differences between the surface energy of small Pt nanoparticles and bulk Pt [15]. As a result of these and other similar findings, there is increasing agreement that Pt dissolution dominates ECA loss in certain

potential regimes through a combination of loss of Pt mass to the ion conductor and dissolution driven particle growth, the mechanisms for which are described in detail below.

Illustrated in Figure 2.2b, ECA loss due to dissolution and re-precipitation (D&R) results from the dissolution of Pt to form Pt^{x+} ions that diffuse into the ion conductor and re-precipitate by oxidizing hydrogen molecules that have crossed over from the anode, thereby forming electrochemically inactive Pt particles both in the ionomer phase of the cathode and outside of the cathode in the membrane [15]. TEM characterization of cycled MEAs has revealed single crystalline particles present in the ionomer and in the membrane [15]. Pt in the membrane generally manifests as a dense band of Pt adjacent to the cathode membrane interface [15].

Ostwald Ripening

As shown in Figure 2.2c, ECA loss due to growth via modified electrochemical Ostwald ripening (MEOR) results from dissolution of the smallest particles in a sample to form Pt^{x+} ions, diffusion of these ions through the ionomer phase, and subsequent redeposition onto the largest particles of the sample [15]. The driving force for this growth mechanism is reduction of surface energy such that the ratio of surface area to volume decreases for large particles by gaining Pt mass from the preferential dissolution of less stable small particles. What role MEOR plays in the coarsening of carbon-supported Pt nanoparticles has been an ongoing question in the literature.

Due to the kinetics of Pt dissolution, MEOR may be regarded as an active growth mode only at cell potentials greater than 0.7V v. RHE. Furthermore, there is unique evidence that MEOR serves as the dominant cause of ECA loss due to growth at cell

potentials greater than 0.8V. Moreover, the contribution of MEOR to ECA loss due to particle growth is likely to increase with temperature due to the temperature dependence of Pt solubility. Direct evidence for the MEOR growth mechanism comes from the work of Ferreira et al., the results of which are summarized below [27]. With direct evidence of Pt dissolution through the observation of single-crystalline Pt particles in the ionomer, analysis of PSDs in MEA cathodes subjected to 10,000 potential cycles between 0.6V and 1.0V reveals that approximately 2-3 nm initial size Pt nanoparticles in the cathode grow to approximately 10 nm at the expense of the smallest particles in the sample [27]. By showing that the mean particle size of carbon-supported Pt nanoparticles in the cathode does not vary in regions that vary in mass percentage of Pt on carbon due to Pt loss through D&R, Ferreira et al. provide unambiguous evidence for growth via MEOR [27]. Their work fully attributes the growth of particles on carbon to MEOR.

Previous studies have investigated the relative contribution of this growth mechanism to ECA loss by comparing the results of PSDs determined by X-Ray Diffraction (XRD) and/or TEM characterization of aged MEA cathodes to the results to the Ostwald Ripening (OR) single growth mode model developed by Granqvist and Burhman [9, 11, 12, 15, 27, 39]. The OR model predicts that a sample of immobile particles characterized by an initially Gaussian PSD ripened exclusively by the OR mechanism will have a final PSD that exhibits a tail to small particle sizes, a peak at large particle sizes, and a finite maximum particle size, as illustrated in Figure 2.3 [39]. The PSD approach to studying MEOR is subject to a variety of errors, however, and the assumptions of the model do not apply to the cathode of PEMFCs. PSDs from the cathode almost invariably include particles both on and off the carbon support, neglecting that particles in the ionomer do no contribute electrochemically and ripen exclusively via D&R [15]. Moreover, the OR model does not include the effects of loss of Pt mass from

the cathode to the membrane via D&R, providing a source of variability that precludes the application of this model to ECA loss. The assumption by the OR model that only one growth mode occurs also complicates its use in studying ECA loss. By unambiguously identifying a dual growth mode involving both D&R and MEOR in the PEMFC cathode, the results of Shao-Horn et al. render the OR single growth mode model inapplicable to PEMFCs [15].

Particle Migration and Coalescence (PMC)

Illustrated in Figure 2.2d, ECA loss due to growth via PMC results from the formation of a single particle from two or more particles moving on the carbon support, followed by sintering after making contact. PMC serves as the presumed growth mode at low cell potentials, where the kinetics of both Pt dissolution (<0.7V v. RHE) and carbon corrosion (<0.8V v. RHE) are slow relative to the lifecycle of the cell [15]. While observed ECA loss and nanocatalyst growth at low potentials provide sufficient cause to regard PMC as an active growth mode, post-mortem characterizations of electrochemically aged MEAs fail to reveal unique and unambiguous evidence for this mechanism. Indirect evidence for PMC comes from PSDs and high-resolution TEM images from MEA cathodes, but such results are ambiguous and subject to interpretation. Complicating the matter further, the mobility of Pt nanoparticles on a carbon support in low temperature fuel cells is poorly understood, and there is no unique evidence that Pt is mobile on carbon in the range of PEMFC operating conditions.

Previous studies have supported growth via PMC by determining PSDs through XRD and/or TEM characterization of aged MEA cathodes and comparing the results to the PMC single growth mode model developed by Granqvist and Burhman [9, 11, 12, 15, 27, 39]. As illustrated in Figure 2.3, this model predicts that a sample of particles with an

initially Gaussian PSD coarsened exclusively by PMC will have a PSD that is log-normal with volume such that it exhibits a peak at small particle sizes and a pronounced asymptotic tail to large particle sizes, essentially the opposite of the PSD from the OR single growth mode model [39]. Most, if not all, PSDs reported in the literature for PEMFCs exhibit a PSD in agreement with the single growth mode PMC model. As with MEOR, however, the PSD approach to studying PMC is subject to a variety of errors. PSDs determined by XRD include off support particles in the ionomer, which do not contribute electrochemically due to their lack of contact with carbon. TEM provides the unique ability to analyze the growth of carbon-supported nanoparticles, but PSDs from aged MEA cathodes determined by TEM have been known to include particles in the ionomer. In one such study, Shao-Horn et al. demonstrate that the peak at small sizes corresponds to particles on the carbon support and that the tail to large particle sizes becomes increasingly pronounced with increasing mass fraction of Pt particles in the ionomer [15]. The unambiguous identification of multiple growth modes operating simultaneously to yield log-normal PSDs renders the single growth mode PMC model inapplicable to PEMFCs.

Another source of indirect evidence for ECA loss due to PMC comes from TEM observations of agglomerates in the cathodes of aged MEAs [15]. Necked nanoparticles represent a stage of sintering, so such particles may very well result from PMC. However, Shao-Horn et al. have proposed another formation mechanism for such nanoparticles involving the deposition of soluble Pt species on immobile Pt nanoparticles in close proximity to one another [15]. Moreover, another likely formation mechanism for agglomerates involves detachment of Pt nanoparticles due to corrosion of the carbon support at potentials greater than 0.8V v. RHE. Because the range of possible formation mechanisms cannot be decoupled ex-situ, TEM characterization of agglomerates in the

cathodes of aged MEAs reveals no interpretable information about the relative contribution of the PMC growth mechanism to ECA loss.

There is no unambiguous evidence that Pt is mobile on carbon in the range of operating conditions, and theoretical modeling has failed to yield results that agree with existing gas phase sintering data [15]. A theoretical approach to PMC comes from Chen and Chan, who employ molecular dynamics simulations for Pt nanoparticles less than approximately 3 nm on a defect-free graphite support [40]. The fact that their results differ by several orders of magnitude from gas phase sintering data has raised the possibility that carbon support defects serve as trapping sites that restrict particle mobility [41]. While theoretical trapping models of gas phase sintering bridge the gap between modeling and existing data, such results offer little insight into particle mobility in the aqueous environment of the PEMFC [15]. The current state of understanding about particle mobility precludes even qualitative comparisons of diffusion constants between samples with different particle sizes, varying degrees of graphitization of the carbon support, or operating parameters such as temperature, relative humidity, and upper potential limit.

This work investigates the role of degradation mechanisms by characterizing the PSD before and after potential cycling and by determining the amount of Pt lost to the cathode membrane interface. Changes in the PSD are attributable to an unknown combination of Pt dissolution and coalescence. The mass percentage of Pt lost to the cathode membrane interface may be estimated from TEM measurements, providing a direct relationship between loss of Pt mass and ECA loss.

2.3 Characterizing Particle Size

TEM studies of degradation mechanisms in the cathode of PEMFCs do not follow a common standard in their approach to characterizing particle size. As a result, there are numerous sources of error and variability in studies of coarsening mechanisms in the cathode of PEMFCs, precluding direct comparisons between them. One source of variability involves differences in how studies define and measure particle size. Studies rely on different size metrics or fail to specify which size metric is employed. Even if size metrics are assumed to be common between studies, differences in image acquisition protocols can lead to different PSDs for identical samples simply due to pixel resolution. A second source of variability involves an attempt to use the image projection of a particle to exclude particles that do not appear to have a particular shape, typically a sphere [26]. Even if all studies decide to analyze only circular projections, there is no guarantee that each sample will have approximately spherical particles. Moreover, the approach to selecting circular projections needs to be quantitative in order to be reproducible between studies. Several common shape metrics provide a possible means to standardize the selection of circular projections [26]. It is unclear, however, if their use serves as another source of error in characterizing particle size. A third source of variability involves characterizing particle overlap [26]. Misinterpreting particle overlap may approximately double or halve the sizes of the particles, so different approaches to particle overlap can lead to substantial variations between studies. This work addresses the need for standardization through mathematical modeling, image simulation, and digital image processing.

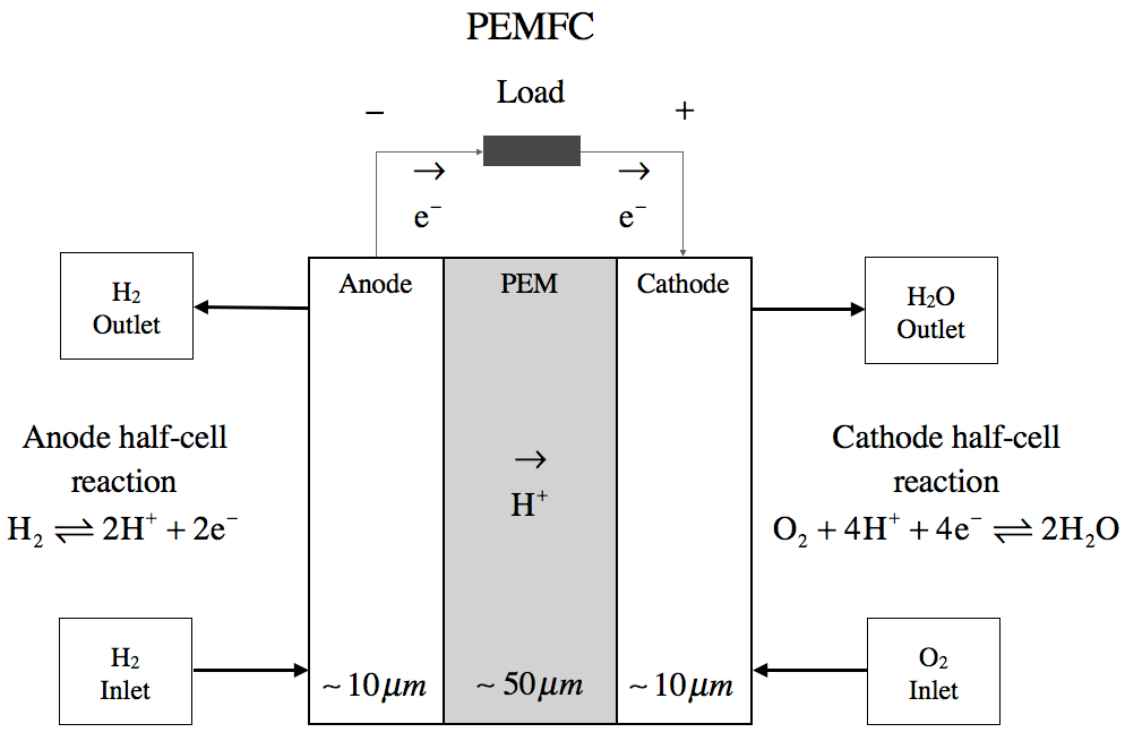

Figure 2.1: Schematic of a proton exchange membrane fuel cell (PEMFC).

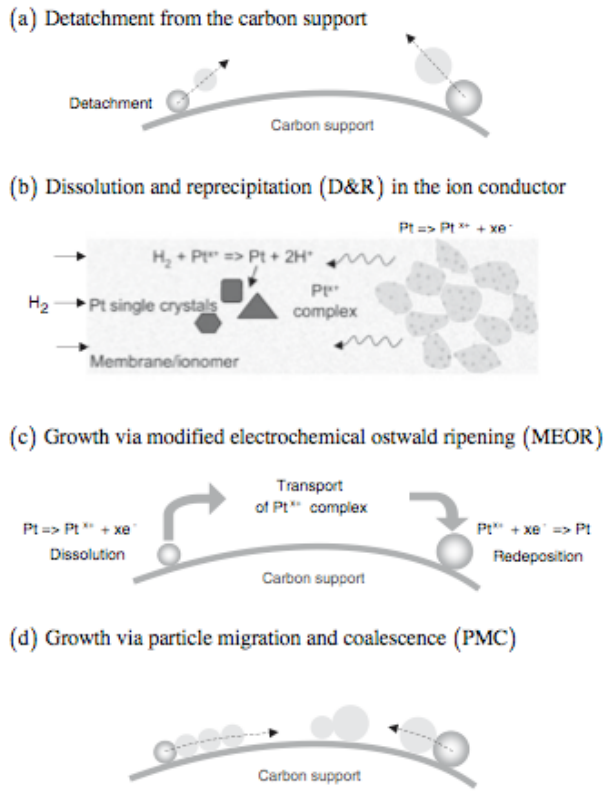

Figure 2.2: Mechanisms of ECA loss in PEMFCs (Adapted from Shao-Horn et al. [15]).

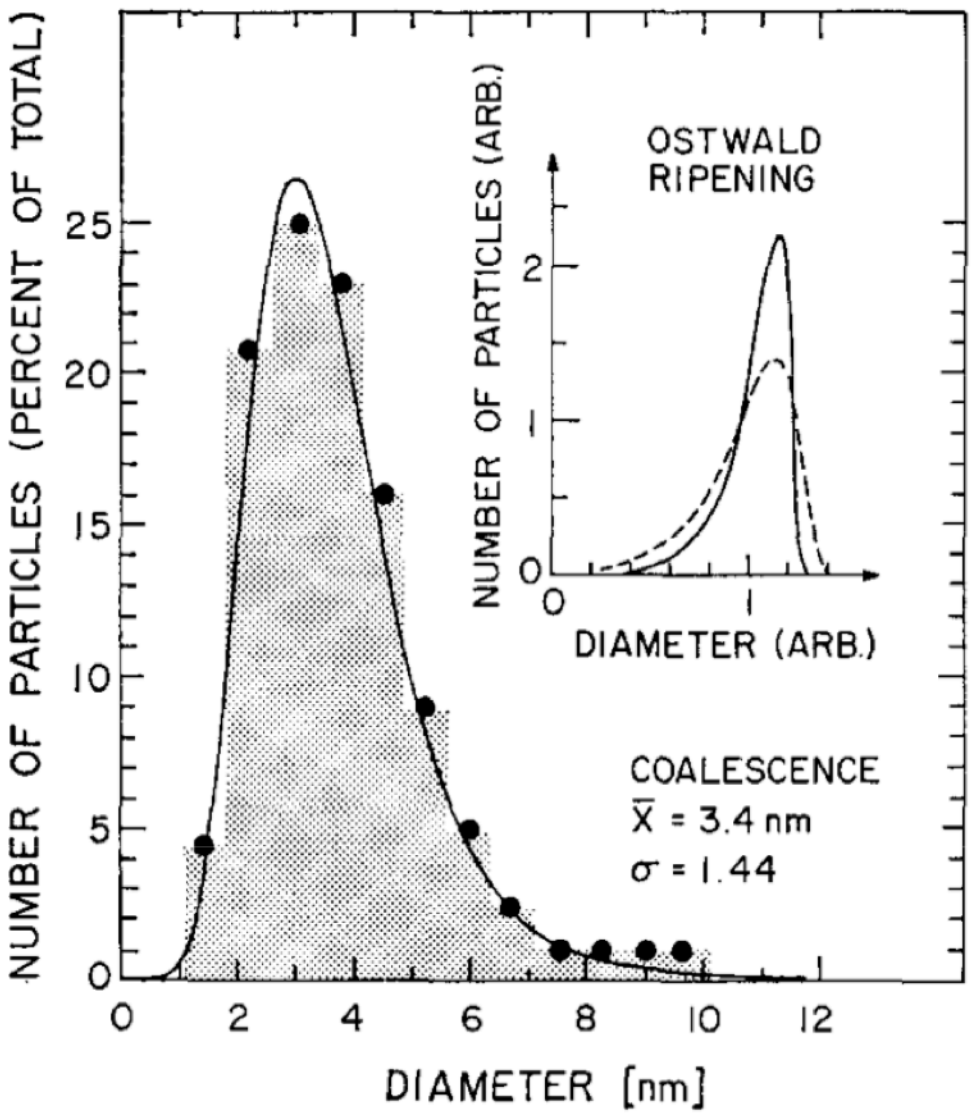

Figure 2.3: Examples of the PSDs from the PMC and OR single growth mode models (Adapted from Granqvist and Burhman [39]).

Chapter 3: TEM for Nanometrology

3.1. Introduction

Nanoparticles have a broad range of technological applications in science and engineering, with many of their most important properties showing a dependence on particle size and shape [42]. In this regard, transmission electron microscopy (TEM) provides a means to characterize nanoparticles based on the cross-sectional projection of particle depending on its orientation with respect to the incident electron beam. However, there are numerous sources of uncertainty in characterizing size and shape in digital TEM micrographs. Factors such as chromatic aberration, spherical aberration, and various sources of astigmatism limit the maximum resolution in a TEM image [43, 44]. Standard approaches to minimize the effects of these sources of variability exist in the form of calibration and alignment protocols [45]. In addition to these instrument-related sources of error, there are also key sources of variability in TEM studies of particle size, which are related with the analysis of TEM images and preclude reproducibility.

The first source of variability involves the definition of particle size. There is little agreement in the actual definition of particle size, with size metrics varying between studies and left unspecified in many cases. Because each size metric provides a unique value for a particular particle size, each has its inherent error as well. There is insufficient quantitative analysis to determine which size metric best meets the needs of TEM for characterizing particle size. Because there is no data that quantifies the error associated with a particular size metric, studies vary in their approach to image acquisition as well. The end result is that error varies complexly between studies due to the use of different imaging modes, magnifications, and definitions of particle size.

The second source of variability involves particle overlap, which introduces error in numerous ways [46]. Particle overlap can render large regions of a TEM image

uninterpretable, leading to sub-sampling through the exclusion of particle sizes that may not be present in other images. Moreover, mischaracterizing two overlapping particles as a single particle introduces a bias to larger particle sizes. Similarly, interpreting a single particle as two overlapping particles introduces a bias to smaller particle sizes. As a result, particle overlap offers potentially the largest source of error in a TEM study of particle size. However, whether an image represents two overlapping particles or a single particle is a matter of interpretation, introducing user bias that varies between studies. There are few studies to date that precisely define how to characterize particle overlap and prevent common root causes of overlap mischaracterization.

The third source of variability involves the use of unproven exclusion criteria to decide which particles to include during image acquisition and analysis. Although TEM studies commonly exclude particles [26], the criteria for exclusion are rarely quantitative and frequently left unspecified. Analysts may differ in their opinions of what constitutes a particular shape, so significant variability may be introduced without a quantitative approach to characterizing particle shape. A typical quantitative approach involves using shape metrics to characterize particles as round, circular, elongated, etc [26]. This approach is so common that popular image analysis software packages such as *imageJ* include programs that give the user the option of automatically excluding particles based on such metrics. However, it is unclear if the use of these size metrics serves as another source of variability. A key requirement for shape metrics is that their ability to distinguish between shapes should be reproducible. This requirement further entails that they show little or no size dependence. The reliability of common shape metrics for exclusion criteria in a TEM study of particle size has not been adequately investigated in the literature.

To address these issues, this paper develops a standard for characterizing particle size and shape that minimizes error and variability. The topics addressed are error inherent to specific size metrics, particle overlap and the use of exclusive criteria.

3.2. SIZE METRICS

Common size metrics rely on an identical formula to characterize particle size, differing only in what quantity is measured for the particle [46]. The general approach for a size metric is as follows: measure a value y of quantity x for a given particle and calculate the diameter of a circle d_x with an equivalent value of y for quantity x. Under this definition, common size metrics fall into three categories based on how they measure a quantity x to calculate d_x. These are the perimeter diameter, area diameter and line diameter.

The "perimeter diameter" measures the perimeter P of a particle and calculates the diameter d_P of a circle that has an equivalent value of P for its perimeter. A circle with diameter d has perimeter given by πd, so the perimeter diameter is calculated by dividing the measured perimeter P of the particle by π, as expressed by

$$d_{\mathrm{P}} = \frac{P}{\pi} \tag{3.1}$$

The "area diameter" measures the area A of a particle and calculates the diameter d_A of a circle that has an equivalent value of A for its area. A circle with diameter d has an area of $\pi\, d^2/4$, so the area diameter is calculated by forming the square of the product of $4/\pi$ and the measured area A. The area diameter is most commonly referred to in the

literature as the equivalent diameter d_{eq}, so the equivalent diameter is calculated according to the expression

$$d_{eq} = \left(\frac{4A}{\pi} \right)^{\frac{1}{2}} \tag{3.2}$$

The line diameter uses the concept of minimum and maximum diameter of a particle. Because the minimum and maximum diameter of a circle equals its diameter d, the maximum diameter d_{max} and the minimum diameter d_{min} are calculated for a particle by measuring the maximum and minimum distances, respectively, formed by line segments connecting the exterior of the particle, as illustrated in Figure 3.1a-b.

Area measurements are preferred in TEM for a variety of reasons. A particle in a TEM micrograph is a projection of a volume, so the number of pixels occupied by the projection represents the limit of certainty about the size of the particle. The projected area of a particle equals the number of pixels within the projection multiplied by a constant representing the scale. The fact that area measurements sample every pixel in a projection has important ramifications for its reliability as a size metric.

To better understand these implications, consider the two possible projections illustrated in Figure 3.1a-b. Area measurements at a given magnification will provide different values for these if and only if they occupy different numbers of pixels. On the other hand, line measurements for the two shapes of different sizes, such as those in Figure 3.1a-b, can have identical values for d_{max} and d_{min}. Perimeter measurements provide different sizes for Figure 3.1a-b, although linear interpolation along the periphery of the shapes introduces a source of variability that precludes its use in TEM studies of particle size.

Area measurements offer another benefit in that they are the least sensitive to noise because they sample the most pixels. To illustrate this effect, consider the example of a single extraneous pixel added to a circle, shown in Figure 3.1c-d. The effect on an area measurement of adding a single pixel to the circle in Figure 3.1c is minimal because there are already 52 pixels in the circle. However, this single pixel increases the maximum diameter by an amount equal to the diagonal length of the pixel. For perimeter measurements, this additional pixel results in an additional 4 edges along which the perimeter must be measured. As a result, line measurements and perimeter measurements show considerable sensitivity to this noise, whereas the effect on the area measurement is minimal. In the example of Figure 3.1c-d, d_{max} and d_P increase by 15% and 11%, respectively, whereas d_{eq} increases by less than 1%.

While these qualitative arguments provide a basis for understanding sources of error, it is unclear how much error is associated with each of the size metrics mentioned above. The ideal projected volume for TEM is an ordinary sphere, so it is important to quantify how reliable a size metric is for the task of finding the diameter of a sphere from its digital projection. Given a sphere with diameter d, a metric gives a value of d_m from the digital projection of the sphere. Thus, the magnitude of the error ε associated with the metric is given by

$$\varepsilon = \left| d_m - d \right| \tag{3.3}$$

Qualitative arguments for the error associated with size metrics have been presented in the literature [43]. The basic premise of these arguments is that there is uncertainty related with the two pixels at the endpoints of the line. However, this approach assumes the line measurement as the size metrics used and thus cannot be applied uniformly to the

three different categories of measurements identified above. Hence, to quantify the error for the perimeter, area and line metrics, simulations of spherical nanoparticles with diameters ranging from 2 nm to 12 nm were conducted with Matlab over an array of bright-field TEM images ranging in magnification from 60kX to 1200kX and subsequently analyzed with *imageJ*.

Figure 3.2 below summarizes the results of these simulations, where the error ε (in pixels) has been calculated from equation 3.3, as a function of the ratio of diameter to pixel size, for each size metric. An increasing value of this ratio represents either increasing the particle size at constant magnification or increasing the magnification at constant particle size. In each case, the abscissa reflects that simulation results are independent if and only if the ratio of diameter to pixel size is unique. Figure 3.2a shows that the equivalent diameter will deviate from the actual diameter by an error value ranging up to 1.8 pixels. Figure 3.2b gives error windows of 1 pixel and 3.3 pixels for d_{min} and d_{max}, respectively. Furthermore, the fact that d_{min} differs from d_{max} in each case constitutes an error in and of itself. Note that the error for the minimum diameter is always lower than that of the maximum diameter in Figure 3.2b because it represents a vertical or horizontal line measurement such that no diagonal error elements are involved. The error for d_{eq} is found to be smaller than that of d_{max} and larger than that of d_{min} for each simulation. Finally, Figure 3.2c illustrates that d_p increases without bound with increasing ratios of diameter to pixel size, a highly undesirable result. This divergence is due to an increasing number of interpolation events along the periphery of the projection. As the number of pixels in the projection increases, the number of pixels in the periphery increases as well, leading to increased number of interpolation events.

Figure 3.2a shows that the equivalent diameter will deviate from the actual diameter by an error value less than 2 pixels. Thus, comparing the equivalent diameter to

the edge length of two pixels provides a reasonable and conservative estimate for uncertainty. Hence, a new parameter is defined, called equivalent error ε_{eq}, based on its equivalent diameter and the pixel size p, which is a function of the magnification M, and expressed as

$$\varepsilon_{eq} = \left[\frac{2p(M)}{d_{eq}} \right] \times 100\% \tag{3.4}$$

The equivalent error accounts for the uncertainty in size measurements arising from the variation in the ratio of particle size to pixel size at different magnifications. This metric provides a standardized means to compare error between samples.

Figure 3.3a shows pixel sizes at selected magnifications for a bright-field 1024 x 1024 pixel image, taken in a JEOL-2010F. These data can be substituted into Equation 3.4 to calculate the equivalent error and compile a series of plots like those in Figure 3.4. These plots can be used during image acquisition to estimate the error associated with particle size measurements at a given magnification. For example, if an image such as the one shown in Figure 3.3b is acquired, which was taken at 120kX, the size of the smallest particle is found to 2.7nm. As can be readily interpolated from Figure 3.4a, equation 3.4 gives an equivalent error of 11.0% for this measurement. Thus, to reduce the equivalent error to, for example, 5%, a linear interpolation of Figure 3.4b shows that the magnification should be increased to 250kX.

3.3 PARTICLE OVERLAP

Figure 3.5 illustrates the dilemma presented by overlapping particles in a TEM particle size study. As shown in Figure 3.5a, it is often difficult to determine the outlines of overlapping particles, forcing their exclusion from the PSD. As a result, particle overlap serves as a common exclusion criterion in image analysis, even when there is little or no uncertainty in the particle outlines, which often leads to sub-sampling. As shown in Figures 3.5b and 3.5c, the probability of overlap increases with particle elongation and increasing particle size, respectively. Excluding such particles skews the PSD to smaller particle sizes and specific particle morphologies. It is also possible to misinterpret two overlapping particles as a single particle or two particles that have coalesced, resulting in their inclusion in the PSD. Reliable image analysis therefore requires a firm understanding of the image formation process for overlapping particles.

To address this need, a mathematical model and a software package have been developed in this thesis to simulate TEM images of overlapping particles. Through a series of simulations where particle size, magnification, and percent overlap are systematically varied, this analysis has identified several root causes of overlap mischaracterization.

To understand the origin of such possible mischaracterization, consider two spherical particles with identical radius R, with particle 1 centered at the origin and particle 2 offset from particle 1 in the xz plane (Fig.3.6). The z coordinates of particle 2 are offset from those of particle 1 by an amount z_0, such that the particles do not occupy the same space, as illustrated in Figure 3.6a. The x coordinates of particle 2 are offset from those of particle 1, such that the diameters of the particles overlap by an amount f, defined as the fractional overlap in the xy plane (Figure 3.6b). The region of overlap in the xy plane of Figure 3.6b, termed the lens region for two overlapping circles, represents

the region of interest in characterizing particle overlap. The coordinates of particles 1 and 2, can be expressed, respectively by equations (3.5) and (3.6),

$$x^2 + y^2 + z^2 = R^2 \tag{3.5}$$

$$\left[x - 2R(1-f)\right]^2 + y^2 + \left(z - z_0\right)^2 = R^2 \tag{3.6}$$

Assuming the beam direction is along the z-axis, the thickness profiles for the particles 1 and 2, can be given, respectively by equations (3.7) and (3.8)

$$t_1(x,y) = 2\sqrt{R^2 - \left(x^2 + y^2\right)} \tag{3.7}$$

$$t_2(x,y) = 2\sqrt{R^2 - \left(\left[x - 2R(1-f)\right]^2 + y^2\right)} \tag{3.8}$$

Finally, the total thickness profile will equal the sum of the thickness profiles of both particles, which can be expressed as

$$t(x,y) = t_1(x,y) + t_2(x,y) \tag{3.9}$$

Note that this relation is valid for any two overlapping particles, regardless of morphology. Assuming that mass-thickness variations dominate, as is the case in HAADF STEM images or bright-field TEM images of particles in the same orientation, the intensity profile in image formation can be linearly related to the thickness profile in Equation 3.9. This represents the most conservative situation in terms of minimizing the

possible errors occurring due to mischaracterization. Obviously, for situations where diffraction contrast dominates, the error is expected to be larger and will not be considered here.

On this basis, Figure 3.6c-e show normalized thickness profiles at three percentages of particle overlap. As mentioned above, the model assumes a linear relationship between the intensity and the thickness profile, which is a good approximation. As evident in Fig. 3.6c, at 10 % overlap, the maximum intensity in the lens is comparable to the intensity at the center of either particle, resulting in low contrast between these points. Because maximum contrast will be acquired between the center of the either particle and the lens outline, the lens detection will point to the case where there is particle overlap, but this can be misinterpreted. On the other hand, Figures 3.6d and 3.6e demonstrate that the intensity at the lens center increases with percent overlap, providing strong contrast to detect particle overlap. These three cases illustrate that a root cause of overlap mischaracterization is assuming that a sharp peak in intensity necessarily accompanies particle overlap. Instead, because it is common to each case in Figures 3.6c-e, the lens outline is the most consistent criterion for detecting particle overlap.

To be able to define a working magnification as a function of particle size and avoid overlap mischaracterization, a program was written in Matlab to simulate bright-field TEM images (1024 X 1024 pixels) of overlapping particles with variable particle size, magnification, and percent overlap. Figure 3.7 displays the results of twenty simulations from this program. Figure 3.7a shows the effect of varying particle size and percent overlap at a constant magnification of 250 kX. The lens regions are readily apparent for all four particle sizes at 25% overlap. Due to sufficient contrast between particle centers and both the lens outline and lens center, an overlap of 15% is also detectable for all but the 2 nm particles. At 10% overlap, the results are very similar to

the case of 15% overlap. Figure 3.7b shows results of eight simulations at varying magnification and percent overlap at a fixed particle size of 4 nm. Overlap percentages of less than 15% were not detectable for 4nm particles at both 60kX and 100kX. Although the contrast is perhaps sufficient at 100kX and 15% overlap, the absence of lens curvature coupled with an increase in lens height makes it more likely to regard these overlapping particles as an instance of coalescence. The remaining simulations demonstrate that lens curvature becomes more apparent at higher magnifications, resulting in more certainty in outline detection.

We are thus left with the issue of detecting the lens outline. To solve this problem, four edge detection methods have been employed, namely the Sobel, Canny, Prewitt and Roberts methods. The best results were obtained using the Sobel edge detection methods and thus the other methods are not presented here. Figure 3.8 shows the results of applying the Sobel edge detection method in Matlab to the source file of Figure 3.7, which are in complete agreement with the analysis of Figure 3.7.

The results from Figures 3.7 and 3.8 yield insight into the root causes of overlap mischaracterization. First, each set of overlapping 2 nm particles in Figure 3.7a illustrate that the likelihood of overlooking the lens region increases as the area fraction of the particles decreases. It is even difficult to see the traced outline in Figure 3.8a for the 25% overlapping 2 nm particles. Second, mischaracterization can occur even when high intensity at the lens center occurs, due to an inability to detect the lens outline, as in Figure 3.7b at 100kX and 15% overlap. Third, distortion in the lens height can make the set of overlapping particles appear coalesced. One remarkable result from Figure 3.7b is that the height of the lens region increases significantly with decreasing magnification, resulting in an apparent neck region that could lead to misinterpretation of particle overlap as an instance of coalescence. This is further investigated in Figure 3.9, which

shows lens elongation for 12% overlapping 3nm particles. The simulation at 500kX provides the geometrically accurate lens height of 1.43 nm. At 100kX, however, the lens height increases by 37% to 1.96 nm. Figure 3.9b shows the pixel intensity profile used to generate the image of the overlapping particles at 100kX, illustrating that this increase in lens height results from intensity spillover from the particle edges near the region of overlap. Similarly, the pixel intensities corresponding to the lens outline are significantly larger than the minimum values given by the thickness profile. As a result of this contrast loss in the lens region and the increase in lens height, these overlapping particles are likely to be mischaracterized as coalesced particles.

3.4 Shape Metrics

There are a variety of metrics used to characterize particle shape. Two common parameters used to characterize shapes, based on curvature and elongation, are roundness and circularity [45]. A lack of understanding about these metrics and the errors associated with them can lead to misuse that introduces bias into a particle size or morphology study. Consider first the parameter roundness. It can be expressed as

$$R = \frac{4A}{\pi a^2} \tag{3.10}$$

which defines the particle in terms of its projected area A and the major axis a of an ellipse fitted to the coordinates of its outline. For digital images, the major axis a equals the equivalent diameter of a circle. Using equation (3.2), the parameter roundness can be simplified to

$$R = \left(\frac{d_{eq}}{a} \right)^2 \tag{3.11}$$

It is important to note that another shape metric, the aspect ratio, is defined as the inverse of roundness, so the analysis of roundness here applies by extension to the aspect ratio as well. Now, consider circularity. It can be expressed as

$$C = \frac{4\pi A}{P^2} \tag{3.12}$$

which defines a particle according to projected area and perimeter P. A closer analysis based on equations (3.1) and (3.2) reveals that circularity can be rewritten as

$$C = \left(\frac{d_{eq}}{d_P} \right)^2 \tag{3.13}$$

One benefit of these dimensionless metrics is that, theoretically, they should be size-independent. From Equation 3.10, one can correctly conclude that the roundness of a particle will tend to unity as the shape tends to a perfect circle. It is incorrect to conclude that roundness will decrease for all shapes as they deviate from a perfect circle. In fact, there are an infinite number of particle shapes with unit roundness. Similarly, one might conclude from Equation 3.12 that a particle will have unit circularity if and only if it is a circle. In fact, circularity measurements of circles in digital images never yield unit circularity. The circularity for a square can equal 1, however.

Figure 3.10 demonstrates the curious behavior of these metrics for three dendritic particles with circularity values of approximately 0.3 but roundness values greater than

0.8. The low circularity values are expected because the measured perimeter increases above the equivalent perimeter with the number of discontinuities and inflection points in the particle outline. The reason for the much higher roundness values, on the other hand, is less obvious. A commonality between these particles is that they exhibit a rough degree of rotational symmetry or periodicity in their outlines. For example, rotating the projection in Figure 3.10c by 60° leads to approximately the same projection. Thus, this projection has an approximate six-fold center of rotational symmetry. In fact, any shape with an n-fold center of rotational symmetry will have unit roundness provided that n>2.

To be understand this effect of rotational symmetry on R, consider first that the major axis can be determined by fitting the coordinates of the particle outline to the equation of an ellipse, given in polar coordinates by

$$r(\theta) = \frac{ab}{\sqrt{(a\sin\theta)^2 + (b\cos\theta)^2}} \tag{3.14}$$

Assuming the requirement for an n-fold rotational symmetry axis corresponding to the coordinates of the particle outline is given by

$$r(\theta) = r\left(\theta + \frac{2\pi}{n}\right) \tag{3.15}$$

then, substituting Equation 3.14 into Equation 3.15 gives

$$\frac{a^2 \sin^2\left(\theta + \frac{2\pi}{n}\right) + b^2 \cos^2\left(\theta + \frac{2\pi}{n}\right)}{a^2 \sin^2\theta + b^2 \cos^2\theta} = 1 \tag{3.16}$$

Equation 3.16 reveals that, for a two-fold center of rotational symmetry, an ellipse with $a=b$ cannot be fit to the shape because of the condition given by

$$a^2\left[\sin^2\theta - \sin^2(\theta+\pi)\right] = b^2\left[\cos^2(\theta+\pi) - \cos^2(\theta)\right] = 0 \tag{3.17}$$

In other words, in equation 3.15, both bracketed terms equal zero, regardless of the values of a or b. Thus, a two-fold center of symmetry imposes no constraint on the value of the major or minor axes represented in equation (3.16). The same result applies for the trivial case of n=1. However, for n>2, symmetry constrains the minimization of Equation 3.16 so that $a=b$, as a direct result of the trigonometric identity $\sin^2\phi+\cos^2\phi=1$. Therefore, a 3-fold or higher rotational symmetry axis leads to equal major axes and equivalent diameters such that the particle will have unit roundness.

This result has important practical consequences because roundness and circularity are frequently used to filter data or exclude particles during image analysis. For example, conducting a PSD study focusing only on "round particles" using an exclusion criterion of R>0.8 would include each of the dendritic nanoparticles in Figure 3.10 while excluding significantly elongated particles. Shapes such as squares and equilateral triangles also have unit roundness because they possess 4-fold and 3-fold centers of rotational symmetry, respectively. Thus, roundness and the aspect ratio have

the limitation that they cannot distinguish between shapes as different as circles, squares, triangles, etc.

Using circularity as an exclusion criterion also introduces significant bias into a particle size study. To better understand one of the sources of error, consider the seven orientations of a single truncated octahedron presented in Figure 3.11a. First, it is important to recognize that TEM measurements of particle size vary widely between projections [47]. For example, the equivalent diameter of the particle in projection 3 is 23% larger than the equivalent diameter of projection 1. As a result, size measurements become more representative of the actual particle size as the number of projections sampled increases such that average size tends to the average of all possible projections.

Second, assume the beam direction to be normal to the page, such that the projections will be the edges of each orientation. With an exclusion criterion of C>0.9, only two projections (3 and 5) will be included in measuring the size of this particle. However, the PSD should not exclude any of these projections because the average sizes in Figure 3.11 most closely represent the three-dimensional parameters of the particle. Using such exclusion criteria also precludes comparison between PSDs because orientations will certainly vary between experiments. The values in Figure 3.11b may suggest that setting C>0.8 or some arbitrarily lower value could serve as a useful exclusion criterion. However, as it will be shown next, the analysis must consider other sources of error that may render this metric unreliable for this purpose.

To investigate the size dependence of the circularity metric, circles and squares with widths ranging from 1 to 100 pixels in increments of 1 pixel were added to 1024 x 1024 pixel images in ImageJ. Analysis of circles reveals that circularity varies with particle size (Fig. 3.12) and tends to unity with decreasing size (Fig. 3.12). The trends and noise in Figure 3.12a result from the perimeter calculations present in the denominator of

equation 3.12. Further analysis reveals that the circularity measurements became less noisy and leveled off to a value of 0.9 with increasing size, as opposed to the theoretical value of 1. For squares circularity tends to unity with decreasing size as well, although the theoretical circularity value is given by

$$C_{\text{Square}} = \frac{4\pi x^2}{16x^2} = \frac{\pi}{4} \approx 0.758 \tag{3.18}$$

In fact, additional analysis of squares with edge length x exceeding 200 pixels shows that circularity for squares tends to the theoretical value with increasing square size (Fig 3.12).

In general, Figure 3.12a clearly demonstrates that circularity fails to distinguish between shapes as different as circles and squares over a range of equivalent diameters. For example, in a BF JEOL-2010F image at 60kX, the circularity of a 2.4 nm square will be greater than those of circles with comparable sizes (6, 8, 9, and 10 nm) and all circles exceeding 13nm. Figure 3.12b compares the equivalent perimeter to the values calculated by *ImageJ* as a function of equivalent diameter. Even though the definition of circularity dictates that the values in Figure 3.12b equal the square root of those in Figure 3.12a, this is not the case for small sizes. This deviation from the definition of circularity and the actual program output leads to the presence of a conditional statement in the source code that sets the circularity to unity when the equivalent perimeter exceeds the calculated perimeter. The result is that circularity tends to unity with decreasing particle size for all shapes, not just circles and squares.

This analysis demonstrates that the use of circularity as an exclusion criterion institutes a bias for smaller particle sizes, regardless of particle shape. Careful consideration of the size dependence and noise illustrated in Figure 3.12 is required

before using circularity values in any correlations or attempts to filter data. The significant noise and error in Figure 3.12 result from the inability to depict curvature with square pixels in a digital image. This difficulty institutes the need for interpolation when calculating the perimeter. Figure 3.13 illustrates this interpolation process for a square and a circle. Consider the perimeter of a single pixel with edge size x as shown in Figure 3.13a. Based on the definition of the perimeter of a square, the program should return a value of 4x for the perimeter. This is, however, not the case. *ImageJ* assumes curvature for all edges of a pixel not in contact with another, linearly interpolating between the centers of each pixel edge. Given explicitly and shown as the perimeter of the darker interior square in Figure 3.13a, the value returned by *ImageJ* is approximately 2.8x. This interpolation process leads to the perimeter values calculated for Figure 3.12. *ImageJ* returns a circularity value of 1 for this single pixel, in agreement with neither the definition of circularity in Equation 3.12 nor the theoretical value for a square in Equation 3.18. The circularity value calculated for a single pixel is given by

$$C = \frac{4\pi x^2}{8x^2} = \frac{\pi}{2} \approx 1.571 \tag{3.19}$$

This value serves as an example of the conditional in the source code setting the circularity to unity when it calculates any higher value.

Consider now the more complex case in Figure 3.13b of a digital circle with a width and height of 8 pixels. As before, the outline of the darker interior region represents the surface used by *imageJ* to calculate the perimeter. With 32 edges, the predicted perimeter would equal 32x, far larger than that of a circle. Interpolation follows a linear path along the diagonals of three noncontiguous pixels for the four corner regions

of the circle. Figure 3.13b gives the Perimeter value calculated by *ImageJ* explicitly and as approximately 25x. Similar to the case of a single pixel, *ImageJ* yields unit circularity for this shape.

Equation 3.20 gives the value calculated in this case, noting that area equals the product of pixel area and the number of pixels.

$$C = \frac{4\pi(52)x^2}{\left(8+12\sqrt{2}\right)^2 x^2} \approx 1.05 \tag{3.19}$$

The conditional statement is invoked until the equivalent diameter exceeds 10 pixels, so a circularity value offers no information about the shape of a circular particle smaller than this (~3nm equivalent diameter at 60kX in a 1024 x 1024 BF JEOL-2010F image).

The approach above demonstrates the dependence of common shape metrics on the number of pixels in a projection, without a direct link to the size of the particle imaged. The results of Figure 3.2 can be used to quantify the exact size dependence of these metrics. Figure 3.14 demonstrates that, as the ratio of diameter to pixel size increases, circularity deviates from the theoretical value of 1, tending to a value of 0.9. This result directly establishes particle size as a source of variability for circularity. Circularity deviates from theory because, as illustrated in Figure 3.2, the error window for equivalent diameter is finite, whereas error increases without bound with increasing ratios of diameter to pixel size.

Figure 3.14 also illustrates the size dependence for another shape metric, the elongation factor, defined in Equation 3.20 as the ratio of the maximum to the minimum diameter [45].

$$E = \frac{d_{\max}}{d_{\min}} \tag{3.20}$$

However, the elongation factor is found to be increasingly reliable because it tends to its theoretical value of unity with increasing ratios of diameter to pixel size. This result is attributable to both the maximum and minimum size metrics having finite error windows that decrease in magnitude as the pixel size decreases, as shown in Figure 3.2. The elongation factor has another disadvantage in that it cannot distinguish between shapes that have identical minimum and maximum diameters, such as those shown in Figure 3.1a-b.

The analysis here provides a foundation to develop a shape metric that will be able to meet the task of selecting approximately circular particles. Equation 3.21 defines a shape metric Γ as the ratio of the equivalent diameter to the geometric mean of the minimum and maximum diameter.

$$\Gamma = \frac{d_{\mathrm{eq}}}{\left(d_{\min} d_{\max}\right)^{\frac{1}{2}}} \tag{3.21}$$

The results of Figure 3.2 demonstrate that the size dependence of this shape metric will be acceptable for circles because each size metric in Equation 3.21 has an upper bound on its error. Using the results from the simulations in Figure 3.2, Figure 3.15 illustrates that the size dependence of this shape metric is minor. This shape metric offers a substantial improvement in comparison to the four shape metrics discussed before it. Unlike Circularity, this metric easily distinguishes between large circles and small squares because it provides a constant value of 0.94885 for all squares. Another added benefit

over circularity is that this metric tends to its theoretical value of unity as the ratio of diameter to pixel size increases. This metric has the added benefit that the value of Γ for circles approaches that of a square as the ratio of diameter to pixel size decreases, which occurs because circles become squares in digital images at small values of this ratio. Unlike Roundness, this metric distinguishes between circles and shapes exhibiting an n-fold center of rotational symmetry ($n>3$). Unlike the elongation factor, this metric distinguishes between the shapes in Figure 3.1a-b due to its inclusion of the equivalent diameter, which accounts for the number of pixels in the shape.

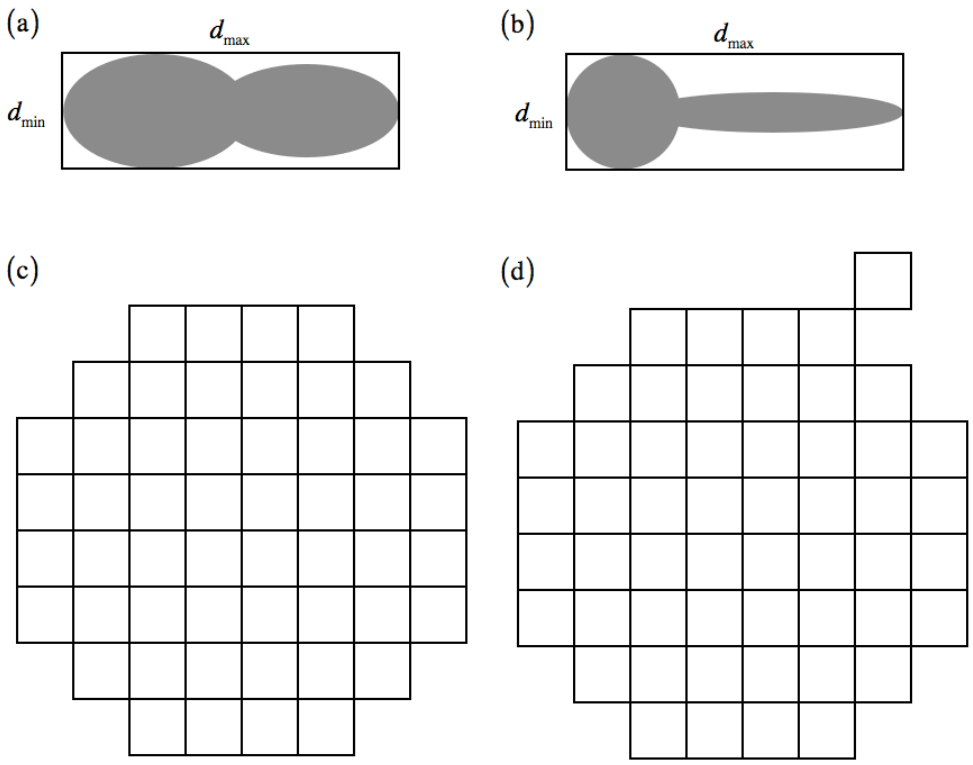

Figure 3.1: Problems encountered by size metrics (a) and (b) illustrate two arbitrary shapes with the same minimum and maximum diameters. (c) depicts a digital representation of a circle 8 pixels in width. (d) depicts the addition of a single pixel to the circle in (c).

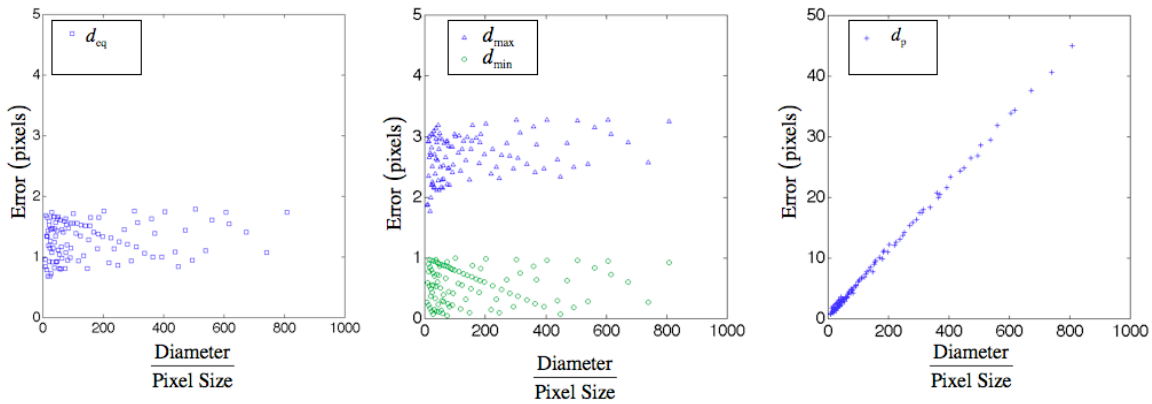

Figure 3.2: Simulation results for the three classes of size metrics. Error as a function of the diameter to pixel size ratio for (a) the equivalent diameter with an error window of 1.8 pixels; (b) minimum and maximum diameters with an error window of 1 pixel and 3.3 pixels, respectively; and (c) the perimeter diameter with an unbounded error window. Based on simulations of spheres ranging in diameter from 2nm to 12nm and JEOL 2010F BF magnifications ranging from 60kX to 1200kX.

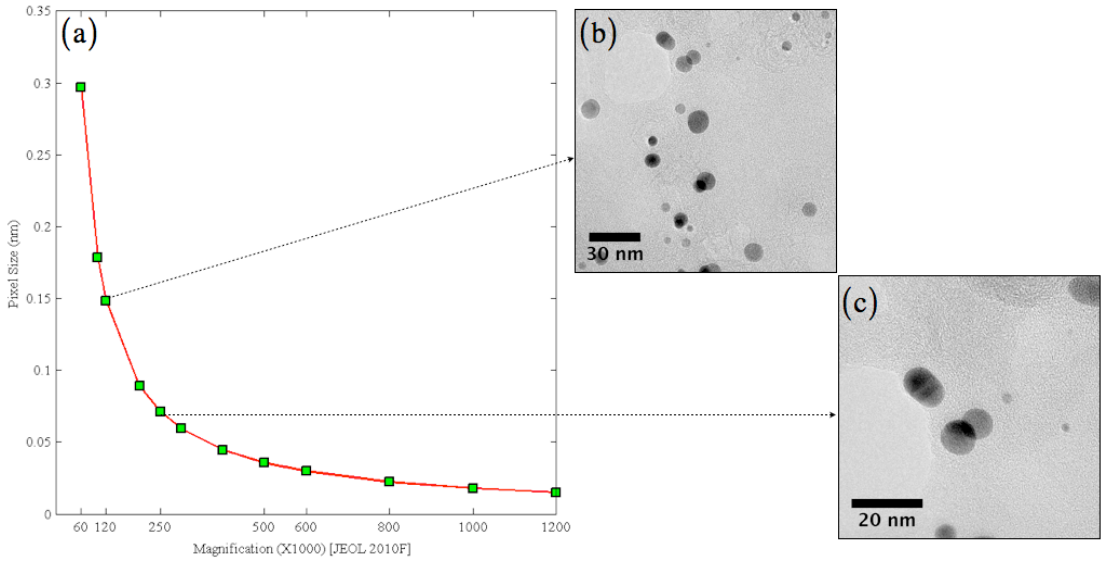

Figure 3.3: Pixel resolution for a BF 1024 X 1024 JEOL 2010F TEM micrograph. (a) Pixel size as a function of magnification for a BF 1024 X 1024 pixel JEOL 2010F image. TEM micrographs of Carbon supported Pt nanoparticles at (b) 120kX and (c) 250kX.

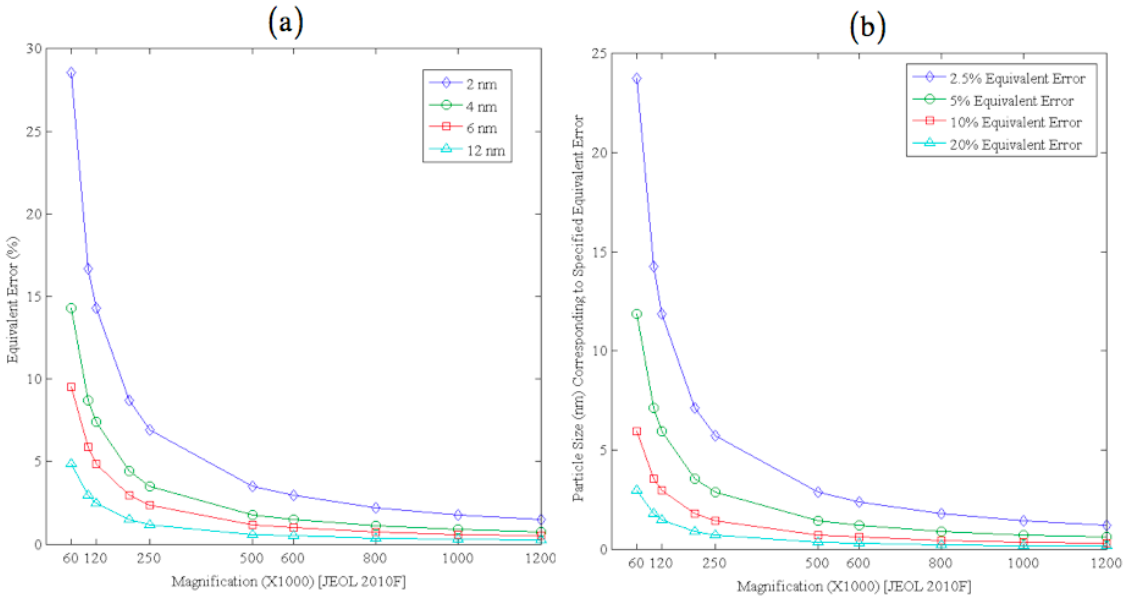

Figure 3.4. A graphical approach to standardized image acquisition based on equivalent error.(a) Equivalent error as a function of magnification for selected particle sizes; (b) Particle sizes corresponding to specified values of equivalent error as a function of magnification. Graphs similar to these or tables with equivalent data serve as tools to minimize error during image acquisition.

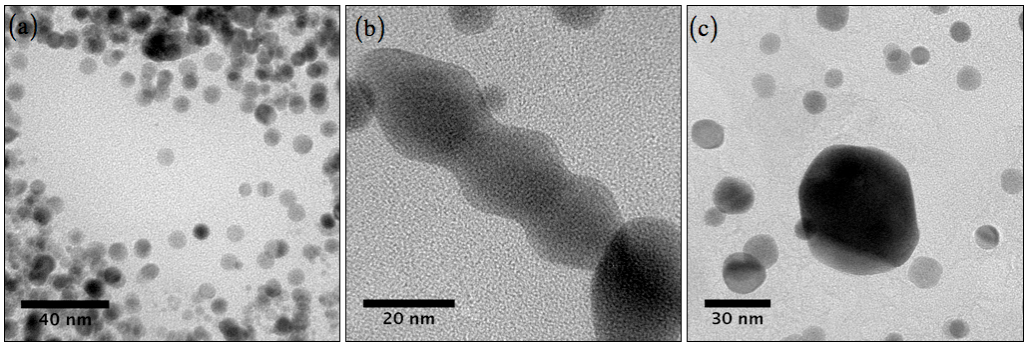

Figure 3.5: TEM micrographs of overlapping Pt particles on a carbon support.(a) Significant overlap often precludes outline detection. Use of particle overlap as an exclusion criterion institutes bias because (b) elongated or (c) large particles are more likely to overlap with other particles.

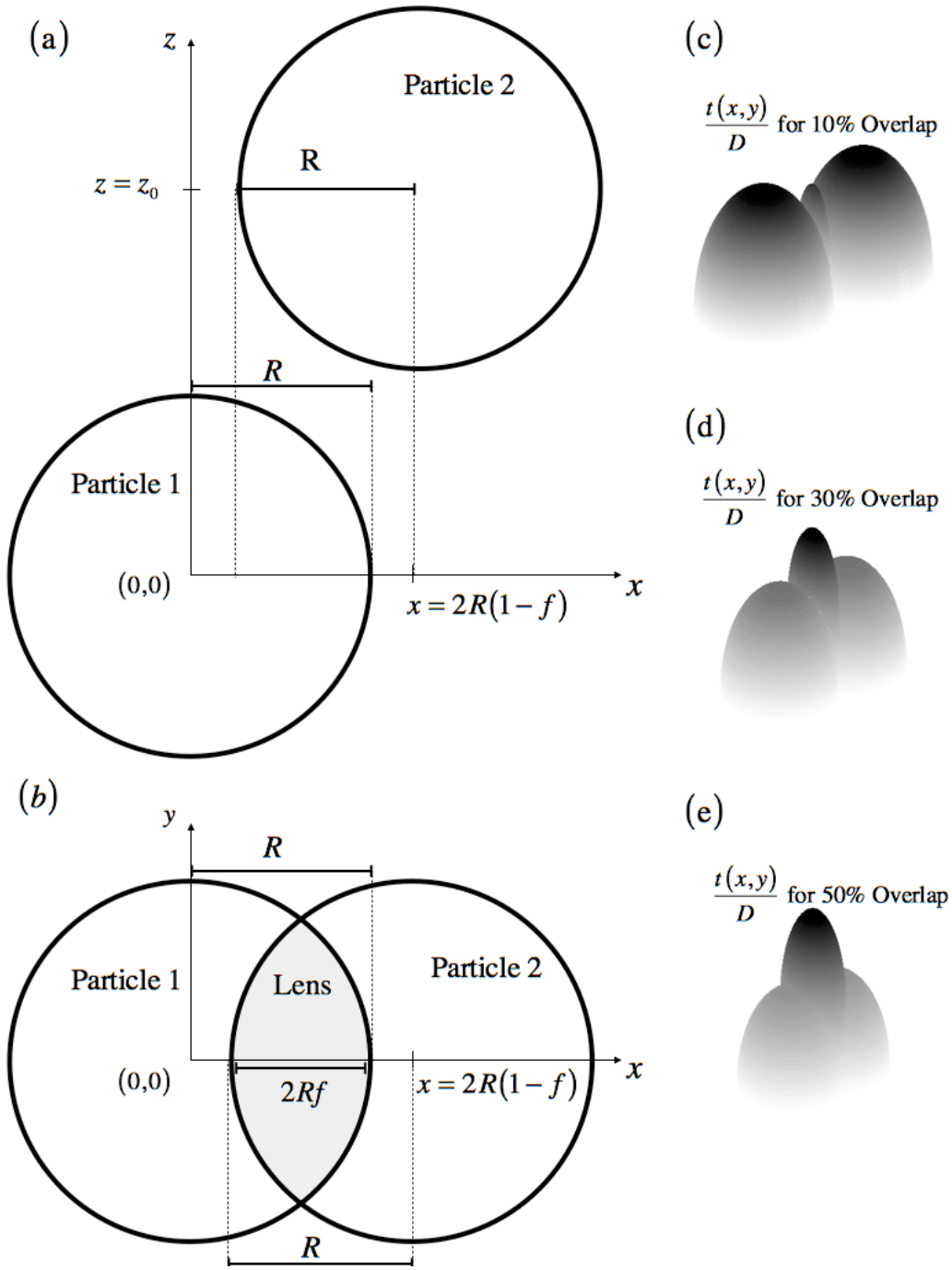

Figure 3.6: A mathematical model for overlapping spheres. Views of the coordinate system from (a) the *xz* plane and (b) the *xy* plane. Normalized thickness profiles for particles with overlap percentages of (c) 10%, (d) 30%, and (e) 50%.

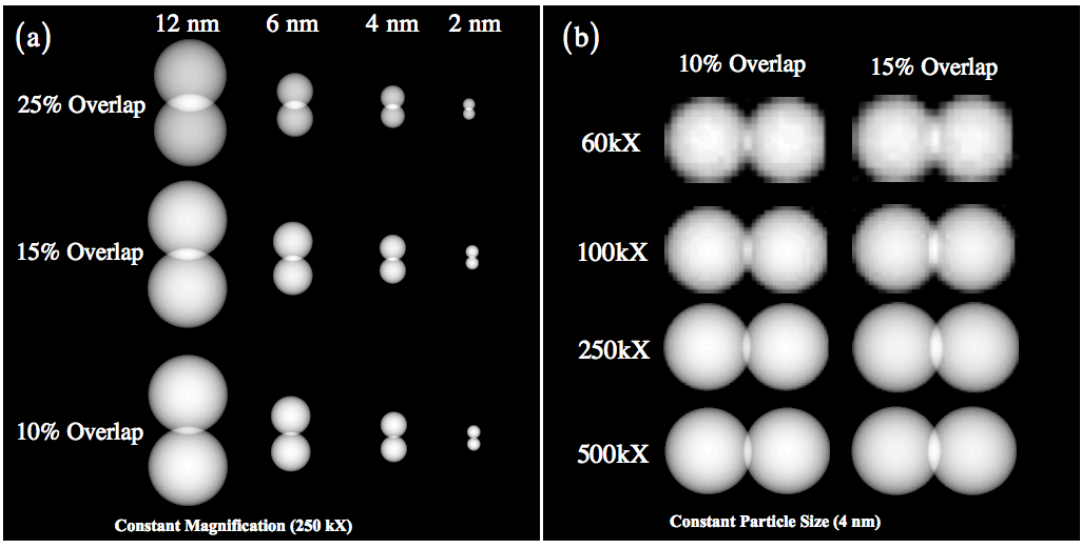

Figure 3.7. Simulation results for overlapping particles.Simulations are for (a) constant magnification with varying particle size and percent overlap and (b) constant particle size with varying magnification and percent overlap.

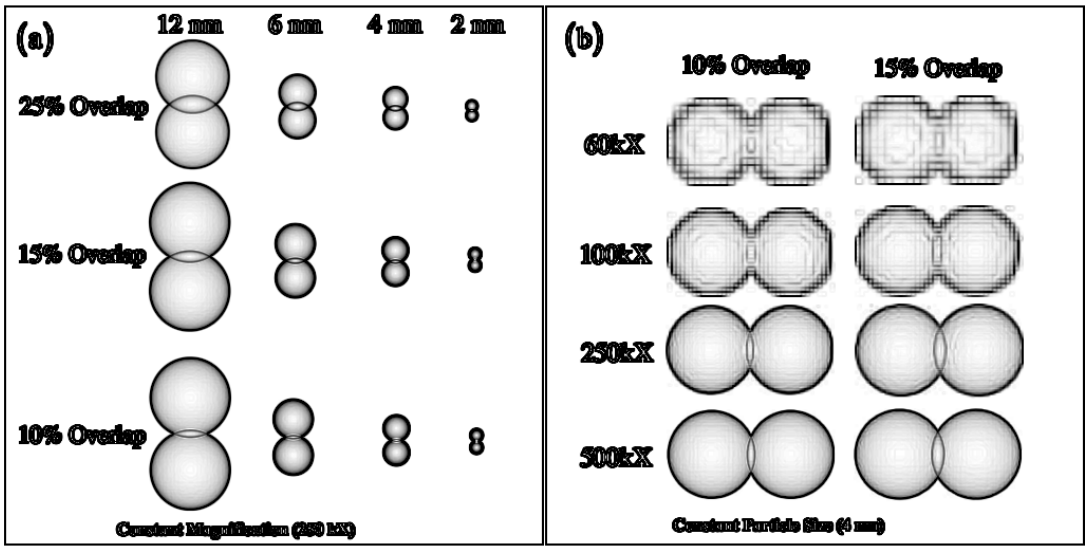

Figure 3.8: Application of the edge detection techniques to simulations of overlapped particles. Results from applying the Sobel edge detection method to the source file of Figure 3.7. In (a), all lens outlines are detected except for the cases of 10% and 15% overlap of 2 nm particles. In (b), lens outlines are not detected until the magnification exceeds 100kX. The Canny, Prewitt, and Roberts methods all detected fewer lens outlines, so their results are not presented here.

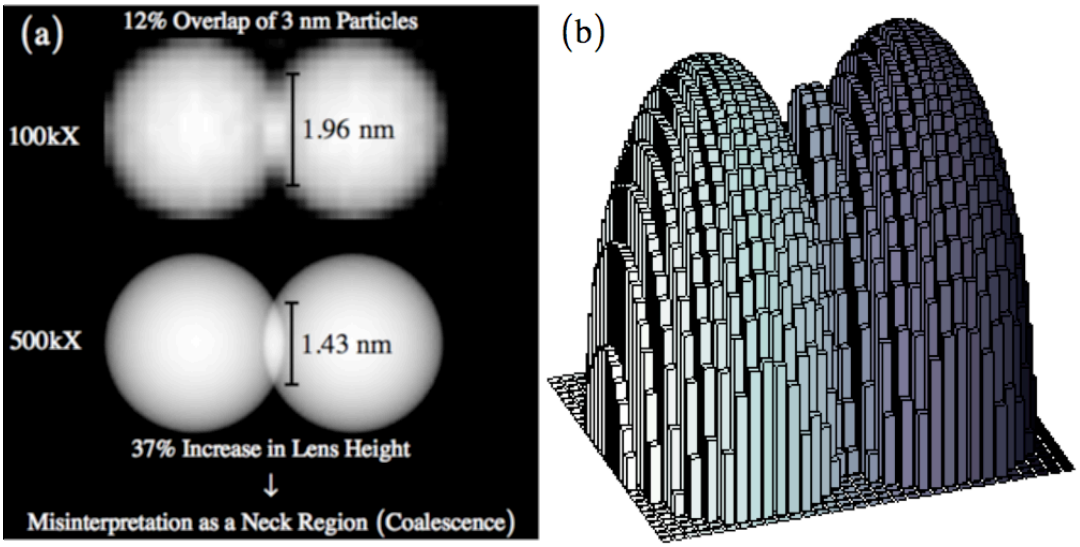

Figure 3.9: Mischaracterizing particle overlap as coalescence. Simulations results for 3 nm particles: (a) mischaracterization of overlapping particles due to the formation of an apparent neck region. (b) Pixel Intensity profile of the mischaracterized particles at 100kX showing nonzero pixel intensity in the region of increased lens height.

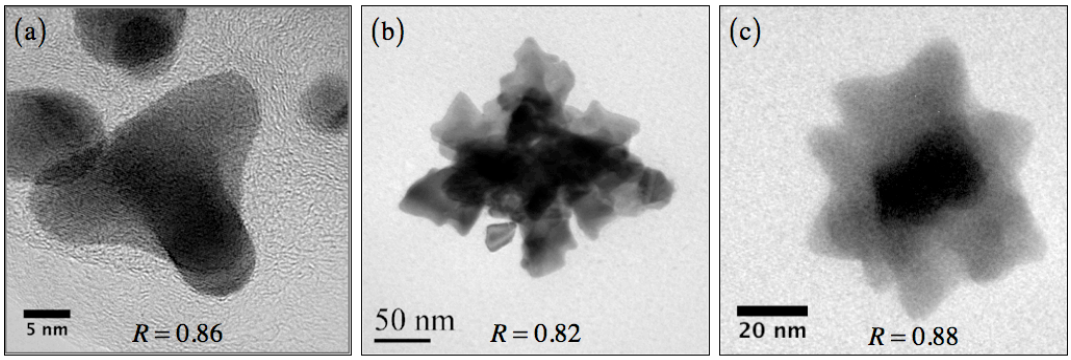

Figure 3.10: TEM micrographs of dendritic nanoparticles. Examples of Pt dendrimers with Roundness values exceeding 0.8 but with low circularity values of (a) C=0.33, (b) C=0.30, and (c) C=0.32. The high roundness values are the result of periodicity in the particle outlines, giving each projection a rough degree of rotational symmetry.

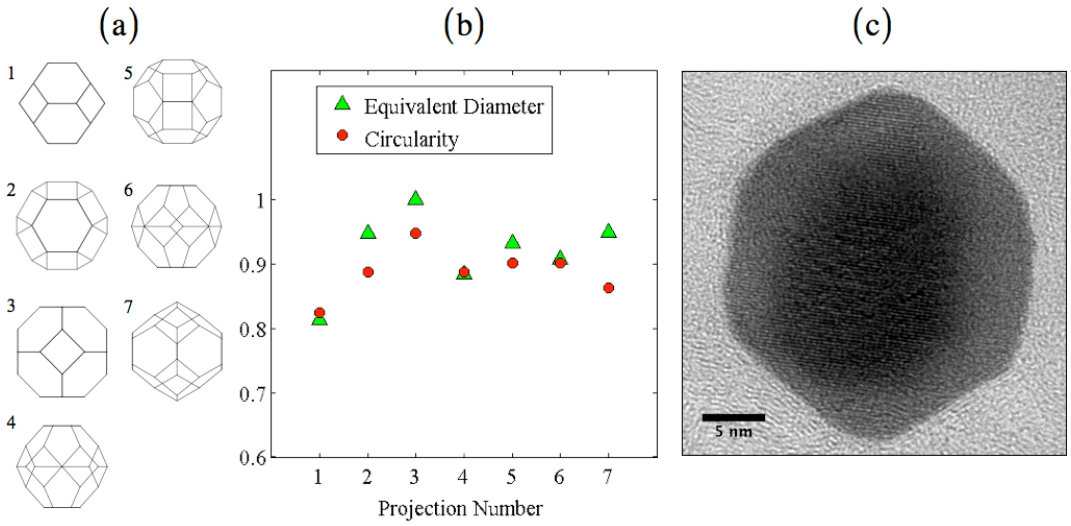

Figure 3.11: The truncated octahedron.(a) Seven orientations of a single truncated octahedron, created by Mathematica [47]; (b) Circularity and equivalent diameter for the seven projections in (a). Equivalent diameters have been normalized by dividing each value by that of projection 3. (c) TEM micrograph of a Carbon supported Pt_3Co nanoparticle exhibiting a morphology similar to projection 6.

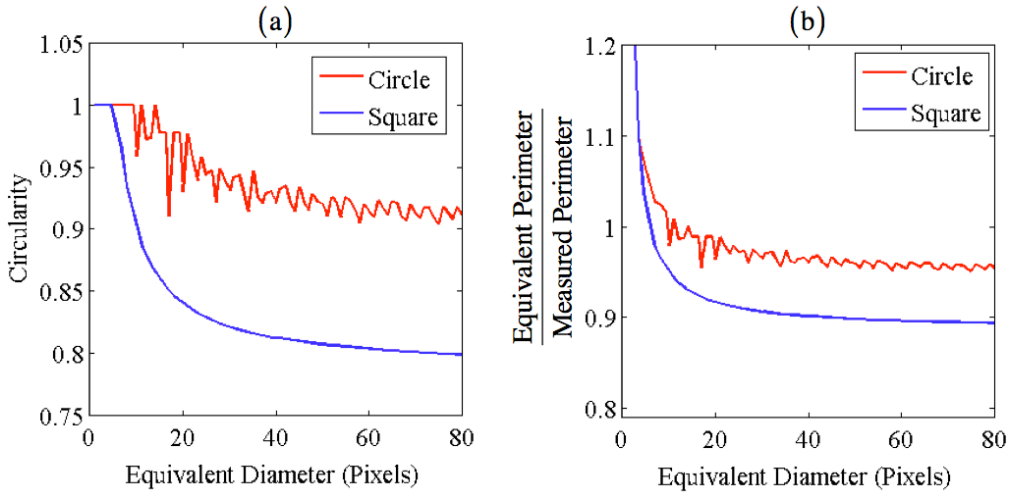

Figure 3.12: The circularity metric for digital circles and squares. Analysis of digital circles and squares generated in single pixel increments to quantify the size dependence of (a) Circularlity and (b) Perimeter measurements.

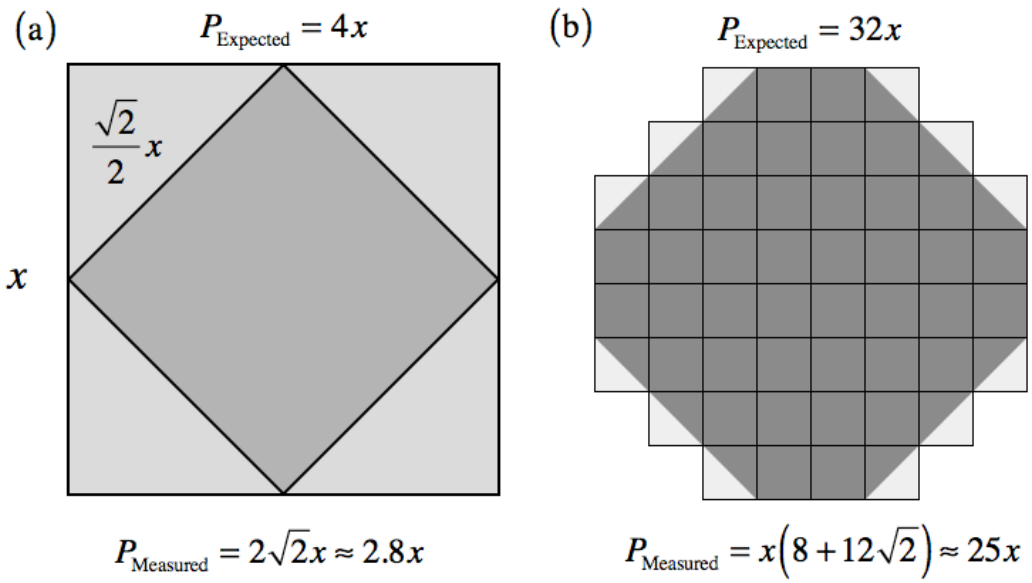

Figure 3.13: Perimeter calculations in digital images.Illustration of perimeter calculations for (a) a single pixel and (b) a digital circle with a width of 8 pixels.

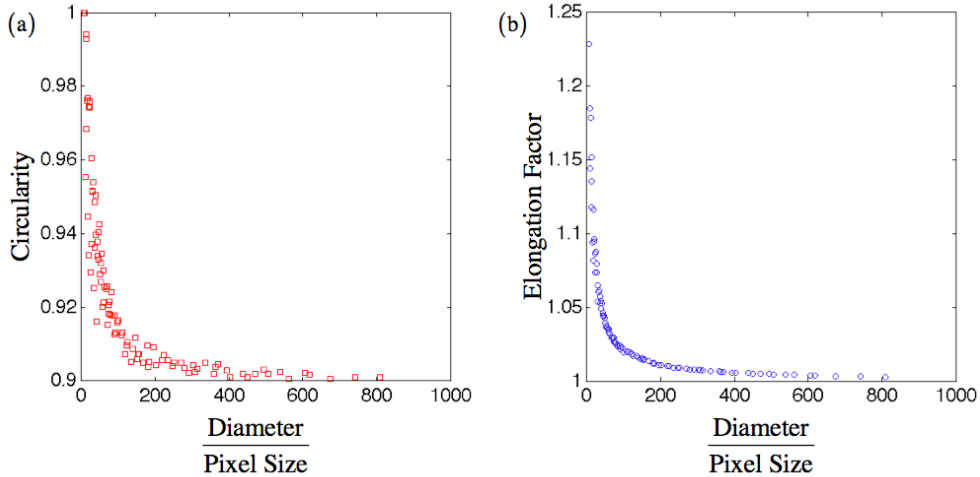

Figure 3.14: The size dependence of circularity and the elongation factor. Simulation results illustrating the size dependence for (a) Circularity and (b) the Elongation Factor based on simulations of spheres ranging in diameter from 2nm to 12nm and JEOL 2010F BF magnifications ranging from 60kX to 1200kX (cf. Figure 3.2). Circularity diverges from and the elongation factor tends to the theoretical value of 1 with increasing values of the diameter to pixel size ratio.

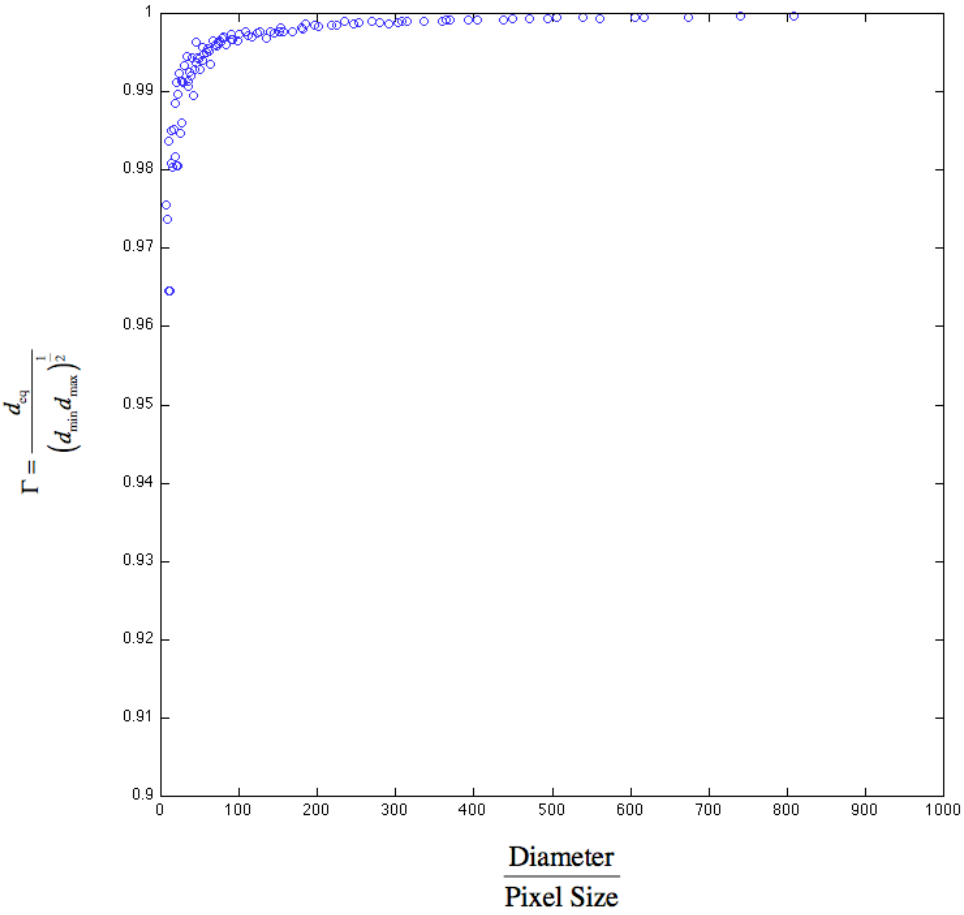

Figure 3.15: The size dependence for Gamma - a novel shape metric. Simulation results illustrating the size dependence for the newly proposed gamma shape factor. Based on simulations of spheres ranging in diameter from 2nm to 12nm and JEOL 2010F BF magnifications ranging from 60kX to 1200kX (cf. Figure 3.2). Gamma exhibits minimal size dependence and tends to its theoretical value of unity as pixel resolution improves.

Chapter 4: The Role of Particle Size on the Performance of PEMFCs

4.1 EXPERIMENTAL PROCEDURE

Materials

This work analyzes three sets of samples corresponding to a range of initial particle sizes to quantify the change in particle size in the cathode throughout the lifecycle of the PEMFC. Four different initial sizes, denoted nominally as 2 nm, 4 nm, 6 nm, and 12 nm, are considered in this study. The first set of samples, herein referred to as "powders", involves the Pt/C powders with different initial particle sizes used to fabricate the cathode materials of the MEAs The second set of samples, herein referred to as the "unused" samples, involves the MEAs fabricated with the Pt/C powder samples before being subjected to electrochemical degradation. The third set of samples, herein referred to as the "used" samples, involves the final products of subjecting the unused samples to potential cycling.

Four Pt/C catalysts with different Pt sizes were chosen to study the influence of initial catalyst size on the various active degradation mechanisms and ultimately the electrochemical performance: (i) a proprietary Pt/C catalyst with a target initial size of approximately 2 nm, 40wt% platinum loading on an Akzo Nobel carbon support, and (ii) the three other Pt/C catalysts prepared by proprietary heat treatment of the abovementioned catalyst to achieve target catalyst sizes of 4, 6, and 12 nm, respectively. MEAs were prepared by coating the catalyst ink and a Nafion ionomer solution onto a decal and subsequently hot-pressing it onto a 25 μm thick Nafion membrane. The anode and cathode catalyst loadings were approximately 0.2 ± 0.02 $mg_{Pt}.cm^{-2}$ and 0.22 ± 0.05

$mg_{Pt}.cm^{-2}$, respectively, with both the electrode layers approximately 10 – 15 μm thick. The cathode was subjected to triangle-wave cycling between 0.6 V and 1.0 V relative to the anode, at a sweep rate of 50 $mV.s^{-1}$ for 10,000 cycles. During testing, MEAs were maintained at 80 °C and 100% relative humidity.

Methods

TEM Preparation of Powders and MEA cross-sections

Samples of Pt-C powders were prepared for TEM characterization by immersing in ethanol, ultrasonicating for approximately 10 s to ensure dispersion, and subsequently depositing on a carbon/copper grid. The morphology of nanoparticles was analyzed with a JEOL 2010F transmission electron microscope operated at 200kV. Unused and used samples were prepared from 5 mm × 2 mm MEA sections cut from the 50 cm^2 serpentine flow MEA test structures. These sections were initially coated with a Gatan-J1 epoxy mixture to improve stiffness, placed in a mold filled with a Araldite® 6005, benzyl dimethylamine and docenyl succinic anhydride mixture, out-gassed to remove air at the MEA/epoxy interface, and cured in an oven at 60 °C for eight hours. The cured molds were microtomed at room temperature with a microtome, and electron transparent MEA cross-sections less than 100 nm thick were obtained. The morphology of nanoparticles present on the cathode side of these electron transparent membranes was analyzed with a JEOL 2010F transmission electron microscope operated at 200kV.

4.2 Results and Discussion

Figure 4.1 contains the Particle Size Distributions (PSDs) obtained from the TEM characterization of the powders used to fabricate the unused MEAs, employing the equivalent diameter d_{eq} as a size metric for 200 nanoparticles in each sample. The

arithmetic mean and 95% confidence intervals are provided for each PSD. Having a mean particle size of 2.1 nm, the 2 nm sample has the smallest breadth of the four powder samples, with the majority of data points between 1 nm and 5 nm. The 4 nm powder sample offers a slightly larger mean particle size of 3.5 nm and a broader PSD, with sizes ranging from approximately 1 nm to 7 nm. The PSD of the 4 nm powder sample is also bimodal, which is attributed to this sample representing an early stage of ripening of the 2 nm sample. With the mean particle size increasing to 6.7 nm and the majority of particles larger than approximately 5 nm, the 6 nm powder sample has a much broader PSD than the two smallest sizes. The 12 nm sample exhibits the broadest PSD and the largest mean of 11.3 nm, although the majority of particles are larger than approximately 5 nm. These data provide a baseline reference for the expected initial performance of each sample. Approximating the ECA as a constant divided by the mean particle size, the initial performance is expected to be highest for the 2 nm sample and lowest for the 12 nm sample.

Figure 4.2 contains the PSDs obtained from the TEM characterization of the cathodes in the unused MEAs. This analysis includes 200 nanoparticles in the region closest to the cathode membrane interface for each sample. Although no data points were collected from other regions of the cathode, particle sizes in the rest of the cathode appeared consistent with those found in the analyzed regions. TEM characterization of the PSDs in the cathode of the unused samples provides a second reference for the beginning of life state of the PEMFC cathode, but it provides an important insight about the state of the PSDs at the end of fabrication. A study of coarsening mechanisms must consider the possibility that MEA fabrication might incur nanocatalyst growth, particularly when comparing samples experiencing only minor growth. Without this step, it is impossible to decouple known growth mechanisms from the possibility of growth

resulting from energy added to the sample during fabrication. The results of Figure 4.2 statistically rule out the possibility of a change in particle size upon fabrication.

Figures 4.3-4.6 contain the results of the TEM analysis of the cycled cathodes. TEM images from three separate regions of the cathode, 3 μm in length, thereby covering the approximate 10 μm electrode width were acquired in a JEOL 2010F operated at 200 kV and analyzed. As illustrated in Figures 4.3-4.6, Regions A, B, and C represent regions of the cathode located 0-3 μm, 3-6 μm, and 6-9 μm from the cathode membrane interface, respectively. A sample size of 200 nanoparticles was chosen for each region of the cathode, leading to a total of 600 nanoparticles for each sample. Although each cathode had regions of the cathode greater than 10 μm, particle size did not appear to vary outside of Regions A-C.

The PSDs in Figure 4.3e-g illustrate that the 2 nm sample attains a mean particle size of approximately 10 nm in each region of the cathode after 10,000 cycles. Differences in the mean particle size between the regions of the cathode are statistically insignificant to 95% confidence. In comparison with Figure 4.1a, the PSD has broadened substantially and shifted from a mean particle size of 2.1 nm to larger sizes, such that the majority of particles are larger than approximately 5 nm. In each region of the cathode, particles remain concentrated between approximately 5 nm and 10 nm. Beyond approximately 10 nm, the PSD exhibit a tail to larger sizes that becomes increasingly pronounced as the distance to the cathode membrane interface decreases.

The PSDs in Figure 4.4e-g illustrate that the 4 nm sample attains a mean particle size of approximately 10 nm in each region of the cathode after 10,000 cycles, similar to the 2 nm use sample. Differences in the mean particle size between the regions of the cathode are statistically insignificant to 95% confidence. Comparison of Figures 4.4e-g and 4.3e-g demonstrates that the mean particle sizes do not differ statistically to 95%

confidence in any region for the 2 nm and 4 nm used MEA cathodes. In comparison with Figure 4.1b, the PSD has broadened substantially and shifted from a mean particle size of 3.5 nm to larger sizes, such that particles smaller than approximately 5 have vanished. In each region of the cathode, particles remain concentrated between approximately 5 nm and 10 nm. Beyond approximately 10 nm, the PSDs exhibit a tail to larger sizes that is most pronounced in Region A.

The PSDs in Figure 4.5e-d illustrate that the 6 nm sample attains a mean particle size of approximately 10 nm in each region of the cathode after 30,000 cycles. Differences in mean particle sizes between Regions A-C are statistically insignificant to 95% confidence. While comparisons of the PSDs in Figures 4.3-4.5 reveals that the mean particle sizes do not differ between the samples of the three smallest initial sizes, it is important to note that the mean for the 6 nm sample represents a value reached by prolonged cycling. In comparison with Figure 4.1c, the PSD has broadened substantially and shifted to larger sizes, such that the majority of particles are larger than approximately 5 nm. In each region of the cathode, particles remain concentrated between approximately 5 nm and 10 nm. Beyond approximately 10 nm, the PSDs exhibit a tail to larger sizes that is most pronounced in Region A.

While the PSDs for the used MEAs of the three smallest initial sizes are very similar, they differ from the PSDs for the used 12 nm MEA because they don't reach the initial mean particle size of the 12 nm sample. The PSDs in Figures 4.6e-g demonstrate that the 12 nm sample attains a mean particle size of approximately 14-16 nm. The mean particle size is found to be statistically equivalent to 95% confidence throughout the cathode. However, substantially more growth has happened in Region A when compared to Regions B and C. Particles larger than 40 nm are common in Region A, whereas they are not observed in Regions B and C. A few particles in excess of 100 nm are observed in

Region A. As a result, the tail to large particle sizes is most pronounced in Region A, similar to the cases of the three smallest sizes.

The fact that the mean particle size does not vary throughout the cathode of each used MEA provides the result that the mean particle sizes from Regions A-C can be averaged for each sample. Figure 4.7 contains the results of this process, comparing the mean particle size of the used cathodes to that of the catalyst powders from which they were fabricated. The change in mean particle size exhibits an inverse proportionality with initial size, and it is found to be statistically significant for each sample. The three smallest samples grow to statistically equivalent mean particle sizes of approximately 10 nm. Both the 2 nm and 4 nm samples have mean particle sizes of approximately 10 nm after 10,000 cycles, whereas the 6 nm sample has a mean particle size of approximately 10 nm after 30,000 cycles. Thus, the 6 nm sample exhibits the lowest growth of the three samples, even though it was subjected to prolonged cycling. The 12 nm sample experiences minor growth, with much of the variability due to the presence of a few large particles in the region closest to the cathode membrane interface.

In addition to growing to the same mean particle size, the trend involving the tail to large particle sizes unites the three smallest initial size samples. There is a direct correlation between the area under the curve of the PSD to the right of a reference particle size and the mass percentage of Pt constituted by Pt nanoparticles greater than this size, which can be estimated from the PSD by assuming spherical symmetry. In Figure 4.3e for Region A of the used 2 nm sample, the tail from 10 nm is more pronounced than it is for Regions B and C in Figures 4.3f and 4.3g, respectively. In other words, the area under the curve of the PSD to the right of 10 nm is greatest in Figure 4.3e for Region A. As a result, nanoparticles greater than 10 nm account for 91% by mass of Pt in Region A, larger than the values of 87% and 84% in Regions B and C, respectively.

For the 4 nm sample, the area under the PSDs to the right of 10 nm for Region A in Figure 4.4e is also largest when compared to Figures 4.4f for Region B and 4.4g for Region C. Similar to the case of the 2 nm sample, the PSDs in Figure 4.4e-g for the 4 nm sample illustrate that nanoparticles greater than 10 nm account for 79% by mass of Pt in Region A, larger than the values of 73% for Region B and 71% for Region C. For the 6 nm sample, the area under the PSDs to the right of 10 nm for Region A in Figure 4.5e is also largest when compared to Figures 4.5f for Region B and 4.5g for Region C. Thus, the PSDs in Figure 4.5e-g for the 6 nm sample illustrate that nanoparticles greater than 10 nm account for 79% by mass of Pt in Region A, larger than the values of 70% for both Regions B and C. With particles growing to more than 100 nm, Figure 4.6e demonstrates that Region A for the 12 nm sample is no exception to this trend. Although the mean particle size does not vary significantly throughout the cathode, substantially more growth has occurred in Region A when compared Regions B and C. The area under the PSD to the right of 16.5 nm, the mean particle size of Region A, is far larger in Region A than it is for Regions B and C. The tail in Figure 4.6e is most pronounced because nanoparticles greater than 16.5 nm account for 96% by mass of the Pt in Region A, as compared to 57% in Region B and 63% in Region C. If particle mobility is assumed to be the same in each region of the cathode, there is no known reason for this large discrepancy to result from growth via particle migration and coalescence. Therefore, the additional Pt mass on large particles in Region A most likely results from Pt deposition. The fact that this trend is present in each sample provides direct evidence for growth via modified electrochemical Ostwald Ripening. Nanoparticles in Region A are exposed to the greatest amount of soluble Pt species due to micrometer scale transport of Pt ions from the cathode to the membrane, leading to more Pt mass being deposited on the largest particles in this region when compared to the rest of the cathode. This trend also

shows the effect of crossover hydrogen, which increases dissolution rates in the region closest to the cathode membrane interface.

Figures 4.8-4.11 contain the mass percentage distributions for each sample, approximated from the PSD by assuming that particles are spherical. For the 2 nm powder sample, particles smaller than 5 nm account for approximately 100% of Pt mass. However, particles smaller than 5 nm account for approximately 0.2% of Pt mass in each region of the cathode of the 2 nm used sample after potential cycling. For the 4 nm powder sample, particles smaller than 5 nm account for 72.3% of Pt mass. However, particles smaller than 5 nm account for approximately 0.2% of Pt mass in each region of the 4nm used cathode after 10,000 cycles. For the 6 nm powder sample, particles smaller than 5 nm account for approximately 4.7% of Pt mass. However, particles smaller than 5 nm account for approximately 0% of Pt mass in each region of the 6 nm used cathode after potential cycling. For the 12 nm powder sample, particles smaller than 5 nm account for approximately 0.2% of Pt mass. However, particles smaller than 5 nm account for exactly 0% of Pt mass in each region of the 12 nm used cathode after potential cycling.

The mathematical modeling and experimental results of Holby et al [30] demonstrate that Pt nanoparticles smaller than 5 nm are substantially more prone to dissolution than larger sizes in potential cycling between 0.6V and 1.0V. This result in conjunction with the analysis of Figures 4.8-4.11 demonstrates that Pt dissolution dominates ECA loss, explaining why particle growth shows an inverse proportionality with initial particle size. Figures 4.8-4.11 demonstrate that there is a driving force to move Pt mass from particles smaller than 5 nm onto particles of larger sizes. With particles smaller than 5 nm accounting for approximately 100% of Pt mass before cycling, the 2 nm experiences the largest change in mean particle size. For the 4 nm sample, particles smaller than 5 nm still account for 72.3% of Pt mass before cycling,

leading to substantial growth that is less severe than the 2 nm sample. The 6 nm sample experiences a smaller change in mean particle size after 30,000 cycles when compared to the 2 nm and 4 nm, which were subjected to 10,000 cycles. This result is directly linked to the fact that particles smaller than 5 nm accounted for less than 5% of Pt mass in the 6 nm sample before cycling. The 12 nm sample experiences the smallest change in mean particle size, and this result is attributable to the fact that particles smaller than 5 nm accounted for only a small fraction of Pt mass before cycling.

It appears from the montages of Figures 4.3-4.6 that Pt loss to the membrane is minor, indicating that the dominant mechanism for ECA loss is particle growth. This observation provides a means to compare the ECA between samples based on the results of Figure 4.7. Figure 4.12 provides a comparison of initial performance and total degradation for each initial size sample, calculating the approximate ECA for each sample by dividing a scalar by the mean particle size and normalizing the results. The 2 nm sample offers the best initial performance. However, it offers the least durability because it experiences a 79% decrease in ECA over 10,000 cycles. The 4 nm sample offers an initial performance that is much higher than the two largest sizes but slightly lower than that of the 2 nm sample. Its high initial performance involves a tradeoff in durability because it experiences a 63% decrease in ECA over 10,000 cycles. After 10,000 cycles, the 2 nm and 4nm samples dropped to approximately the same ECA value, which is lower than the initial performance of the 6 nm sample. The 6 nm sample offers a lower initial performance when compared to the two smallest sizes. However, a substantial improvement in durability accompanies this decrease in initial performance, with the ECA of the 6 nm sample decreasing by only 30% over 30,000 cycles. Even after 30,000 cycles, the ECA of the 6 nm sample has approximately the ECA value attained by the two smallest initial sizes after 10,000 cycles. While the 12 nm sample experiences the

lowest ECA loss of 24%, the initial performance is lower than the final performance of each of the three smaller sizes. Thus, the 6 nm sample represents an ideal initial PSD that balances initial performance and stability.

The presence of specific morphologies illustrated in Figure 4.13 provides further insight into the operating degradation mechanisms. Although most nanoparticles were approximately spherical, two distinct morphologies were found in each specimen: (i) coalesced (Fig. 13a-b) and (ii) dendritic (Fig. 13c). As shown by the FFT in Figure 4.13d, the dendritic nanoparticle is a single crystal. This confirms that the dendritic particles arise from the dissolution and reprecipitation of Pt. The origin of coalesced nanoparticles is less clear, however, as they may arise from a combination of three possible formation mechanisms.

First, coalesced morphologies may result from nanoparticles migrating and coalescing on the carbon support. Second, it is also possible that coalesced particles are the result of particles in close proximity making contact by increasing in size due to Pt deposition. This formation mechanism cannot be ruled out because Pt dissolution and subsequent growth via MEOR are active mechanisms in potential cycling between 0.6V-1.0V, with the upper potential limit exceeding the 0.7V v. RHE threshold for Pt dissolution. A third and likely possible mechanism for particle contact is particle detatchment. This formation mechanism cannot be ruled out because potential cycling exposes carbon to potentials above 0.8V v. RHE, below which the kinetics of carbon corrosion become negligible. None of these formation mechanisms can be identified unambiguously by post-mortem studies, namely because it is impossible to determine what caused particle contact. Consider the case of coalescence via particle migration. Each sample provides evidence that every coalescence event could have resulted without particle migration. The particle in Figure 4.13a from the 2 nm used MEA represents a

binary coalescence event involving two ~9 nm particles, while the particle in Figure 4.13b from the 12 nm used MEA appears to represent a ternary coalescence event involving three ~25 nm particles. Growth via a combination of mechanisms must have occurred before or during the coalescence events in each of these cases because such large sizes were nonexistent in the unused MEAs. Coalescence via modified electrochemical Ostwald ripening is particularly likely in Region A of the 12 nm used MEAs, where particles on an approximately 150 nm carbon aggregate grow to sizes in excess of 100 nm.

Regardless of their precise formation mechanisms, morphologies resulting from aggregation-coalescence represent a form of ECA loss not directly quantified by the PSDs. The widespread presence of necked nanoparticles and cluster agglomerates in each sample provides a means to quantify what percentage of Pt has experienced ECA loss due to the aggregation coalescence mechanism and thus compare the relative impact of this degradation mechanism as a function of initial particle size. To this end, the projected Area (A) of Pt in each image was separated into one of two categories: (1) Pt in the form of individual nanoparticles ($A_{Individual}$) and (2) Pt exhibiting clear aggregation-coalescence ($A_{Coalesced}$). The Pt due to particle overlap was excluded from this analysis but accounted for no more than 10% of Pt for each image. Finally, the minimum percentage of Pt experiencing ECA loss due to aggregation-coalescence was calculated from the ratio of the projected area of coalesced Pt ($A_{Coalesced}$) to the total projected area of Pt ($A_{Total} = A_{Coalesced} + A_{Individual}$). Figure 4.14 contains the results of this analysis, with ECA loss due to coalescence showing the expected trend of increasing severity with decreasing particle size. Additional work is needed to determine the most likely formation mechanism for such particles. The data point for the 6 nm sample in Figure 4.14d requires special attention because it represents 30,000 cycles, whereas the data points for the other sizes

represent samples subjected to only 10,000 cycles. The fact that the 6 nm sample contains more agglomerates than the 12 nm sample therefore reveals no conclusive information. However, the fact that the 6 nm sample had fewer agglomerates than both the 2 nm and 4 nm samples after extended cycling underscores that this sample offers substantially greater durability when compared to the two smallest sizes.

Figure 4.15 demonstrates that the effect of Pt loss through dissolution and reprecipitation in electrochemically inaccessible regions of the cell follows the expected trend of decreasing severity with increasing size. Pt loss to the membrane, however, offers only a minor contribution only to ECA loss because the mass percentage of Pt lost to the membrane ranges from 0.4% in the 12 nm sample to only 9.0 % in the 2 nm sample. This low percentage of Pt loss is attributable to the small amount of crossover hydrogen. Therefore, ECA loss results primarily from nanoparticle growth through a combination of aggregation-coalescence and modified electrochemical Ostwald Ripening. This observation validates the approach of Figure 4.12, which assumed particle growth dominated ECA loss. The image in Figure 4.15d for the 6 nm sample requires special attention because it represents 30,000 cycles, whereas the images for the other sizes represent samples subjected to only 10,000 cycles. The fact that the 6 nm sample shows a higher amount of Pt in the membrane than the 12 nm sample therefore reveals no conclusive information. However, the fact that the 6 nm sample had a higher amount of Pt in the membrane than both the 2 nm and 4 nm samples after extended cycling underscores that the role of dissolution and reprecipitation is substantially more dominant for the two smallest sizes. The 6 nm sample therefore offers greater stability than the two smallest sizes in that it experiences less ECA loss due to loss of Pt mass to the membrane.

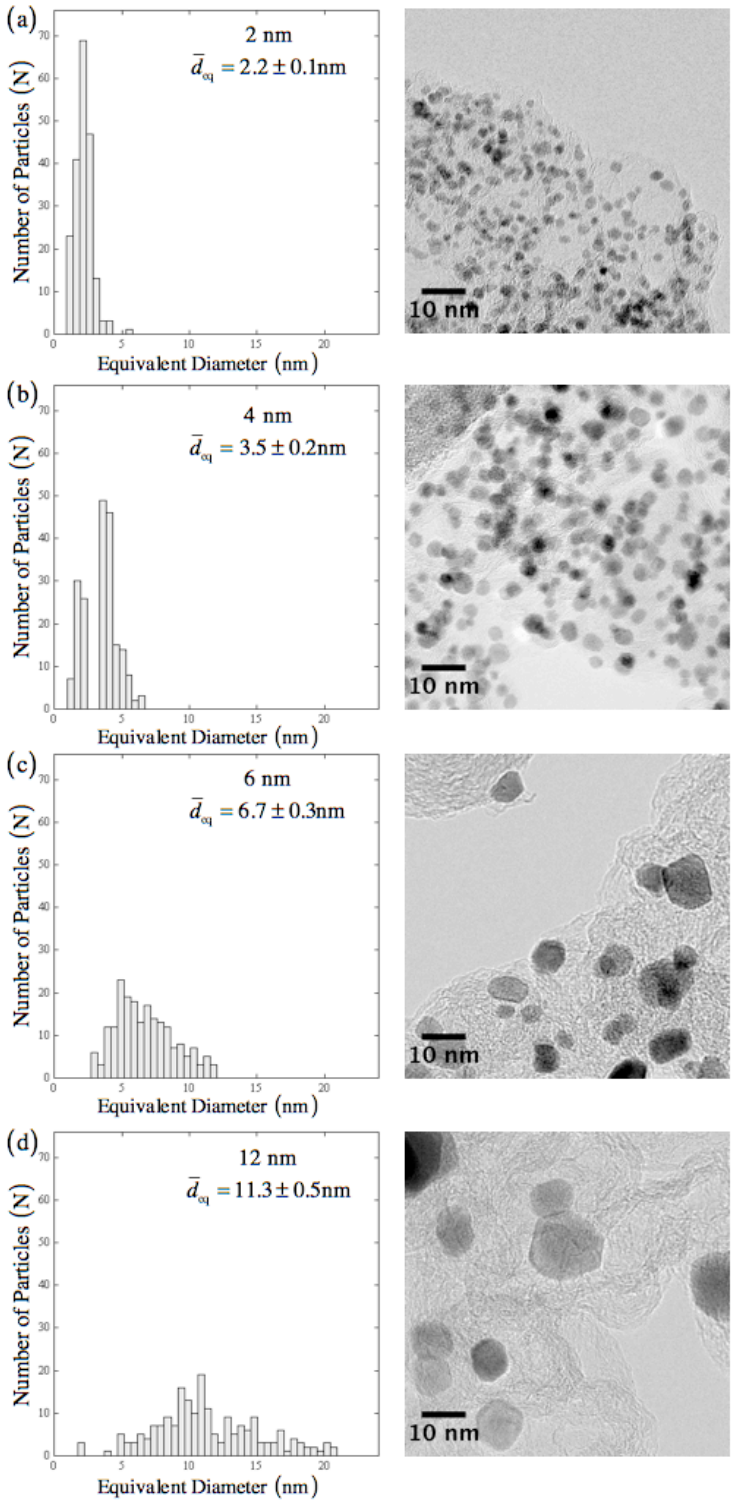

Figure 4.1: TEM characterization of the PSDs for the powder samples.

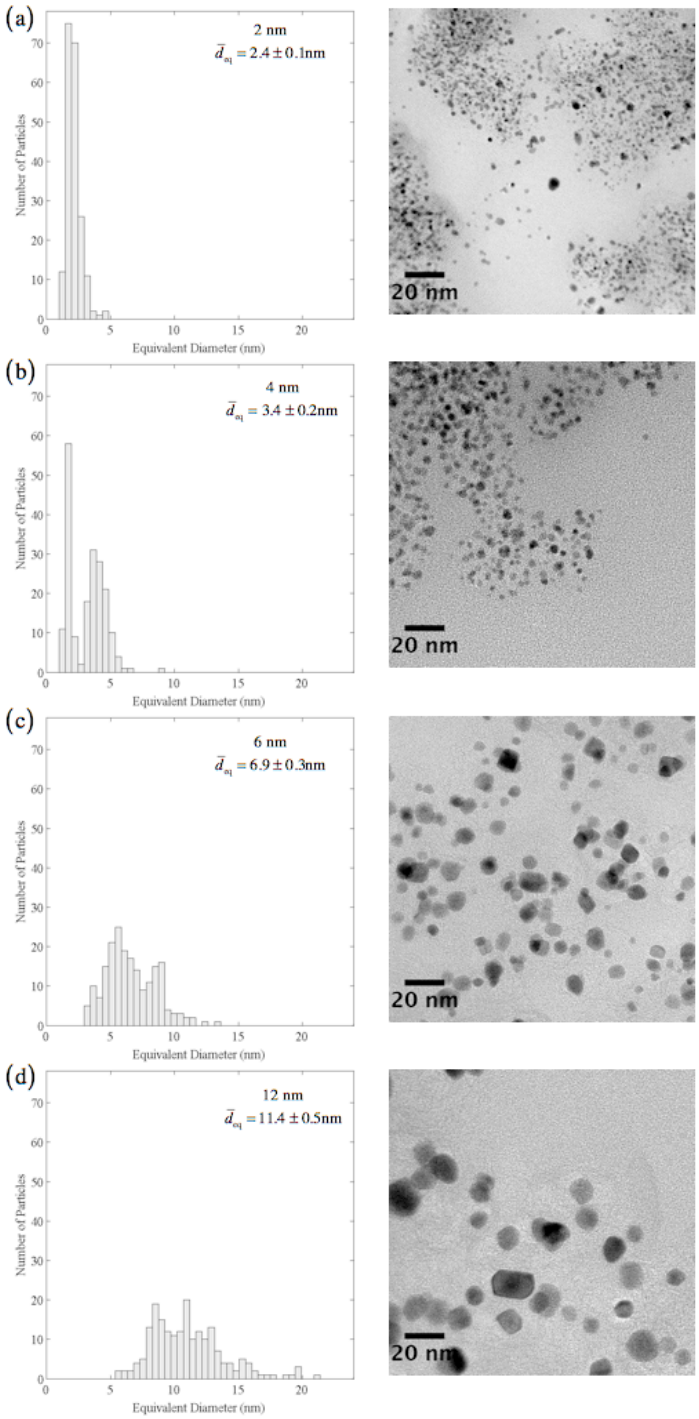

Figure 4.2: TEM characterization of the PSDs for the unused samples.

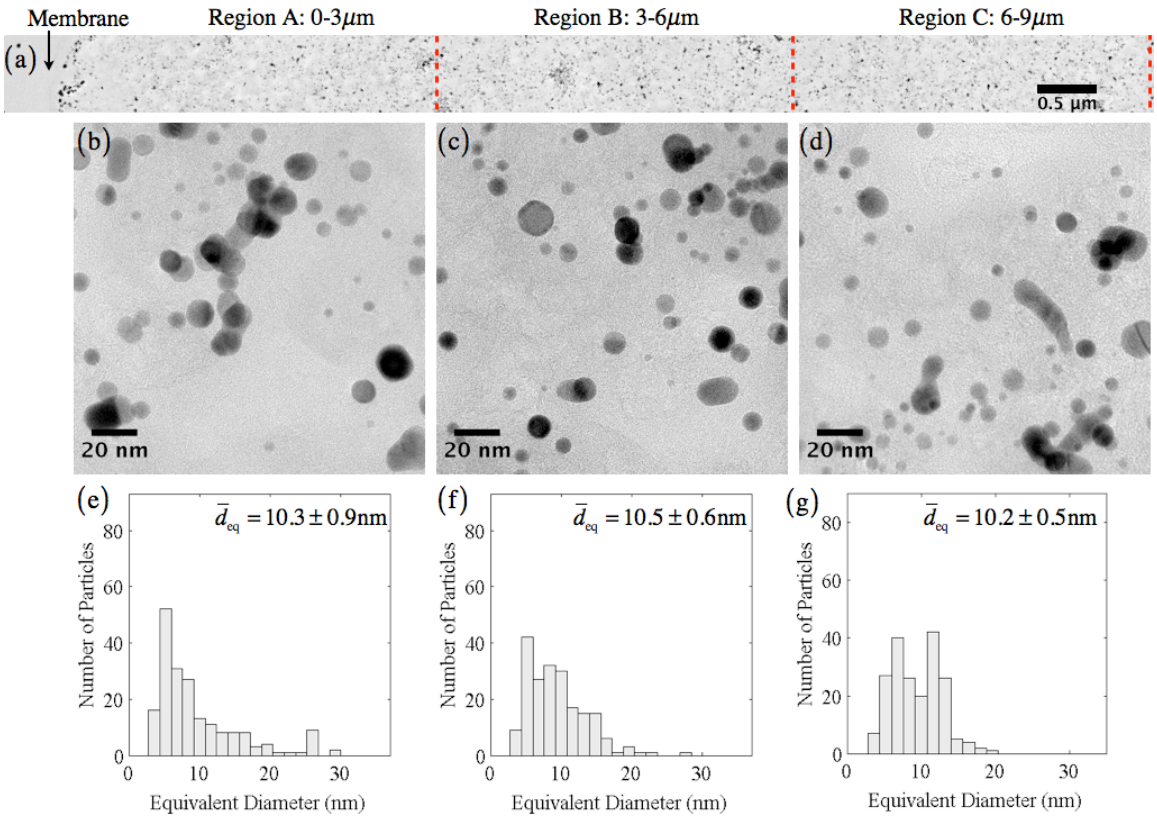

Figure 4.3: TEM characterization of the used 2 nm sample.

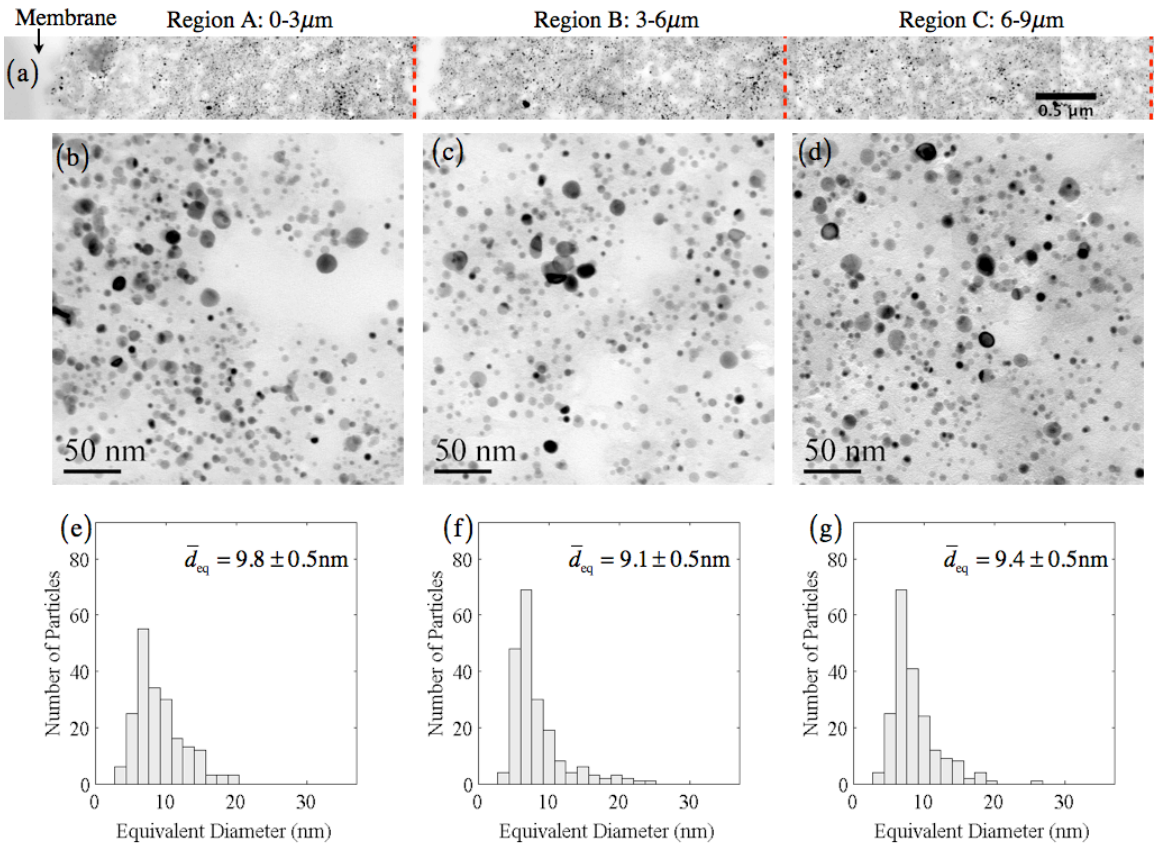

Figure 4.4: TEM characterization of the used 4 nm sample.

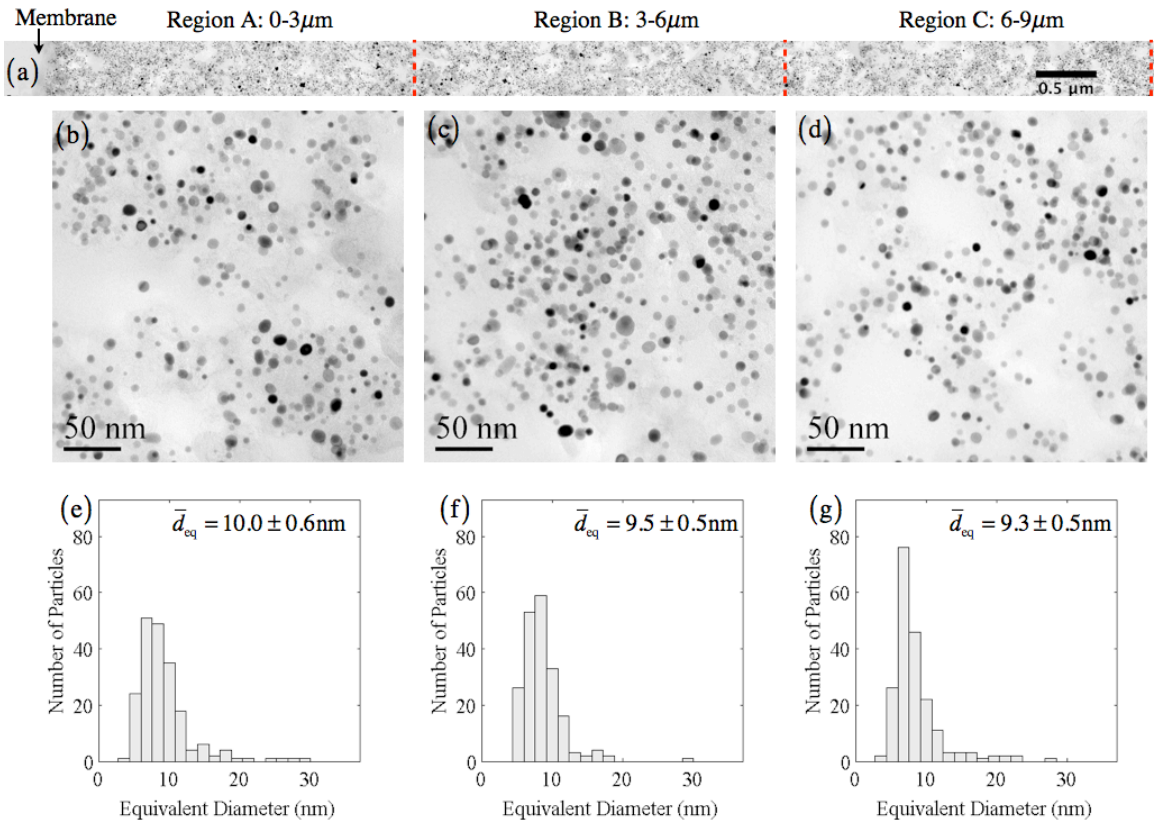

Figure 4.5: TEM characterization of the used 6 nm sample.

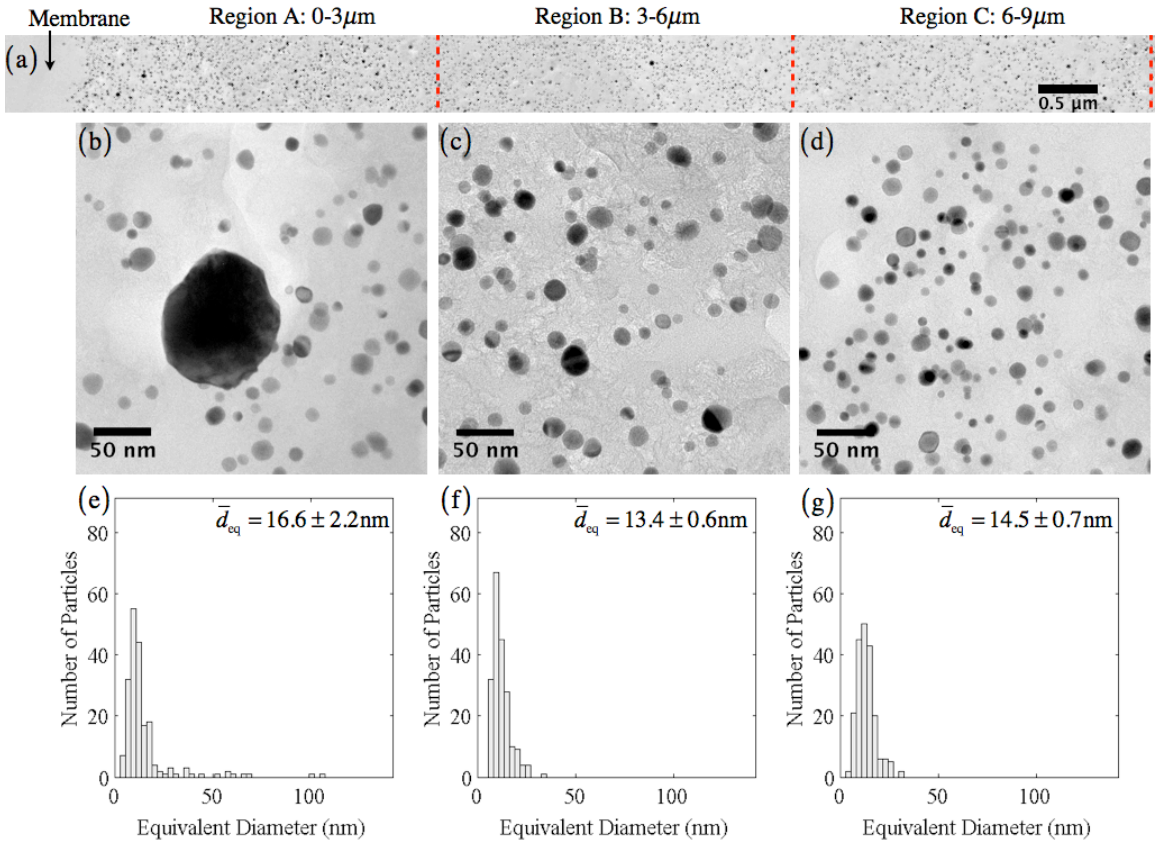

Figure 4.6: TEM characterization of the used 12 nm sample.

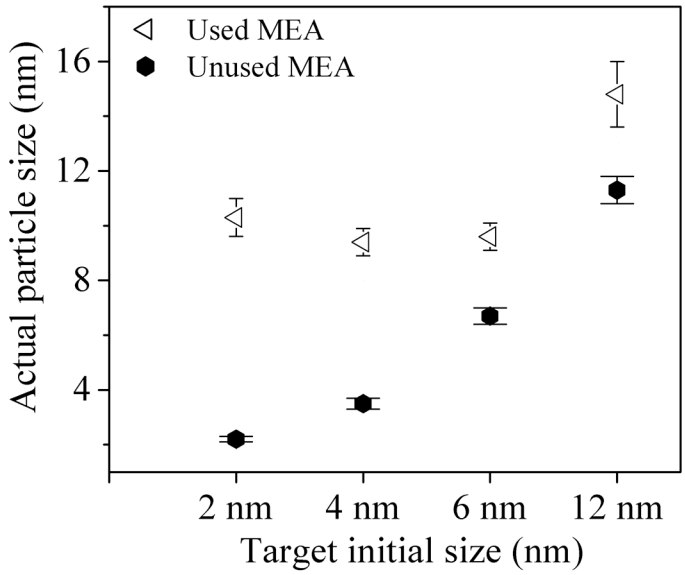

Figure 4.7: Changes in mean particle size upon cycling.

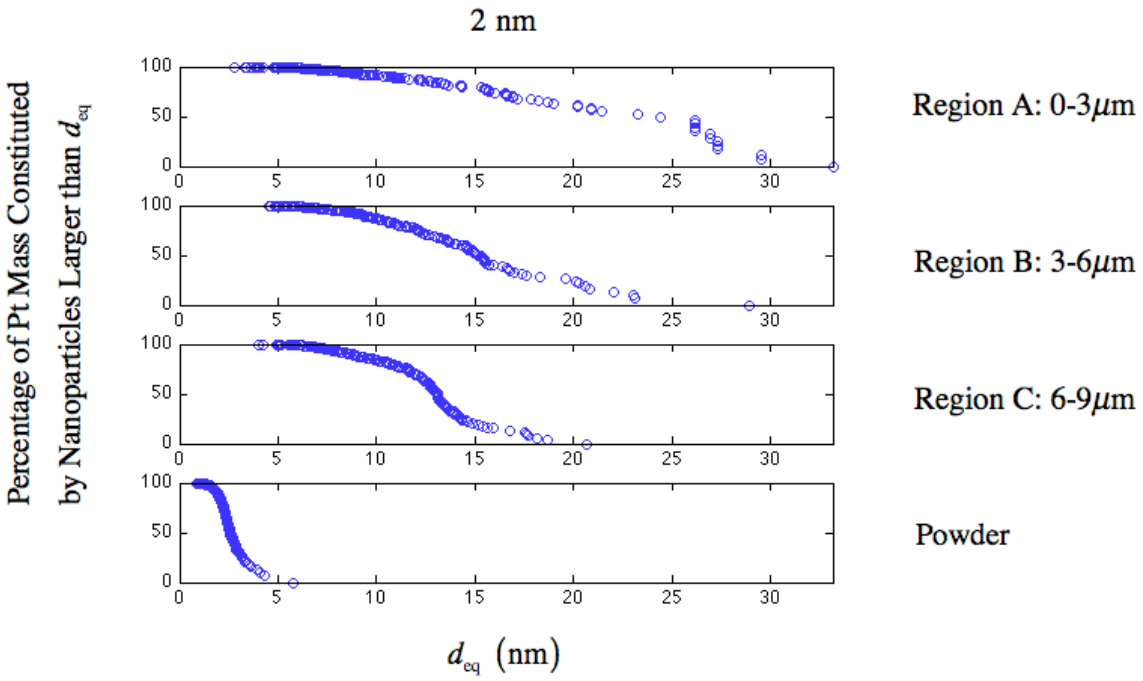

Figure 4.8: Mass percentage distributions for the 2 nm samples before and after cycling.

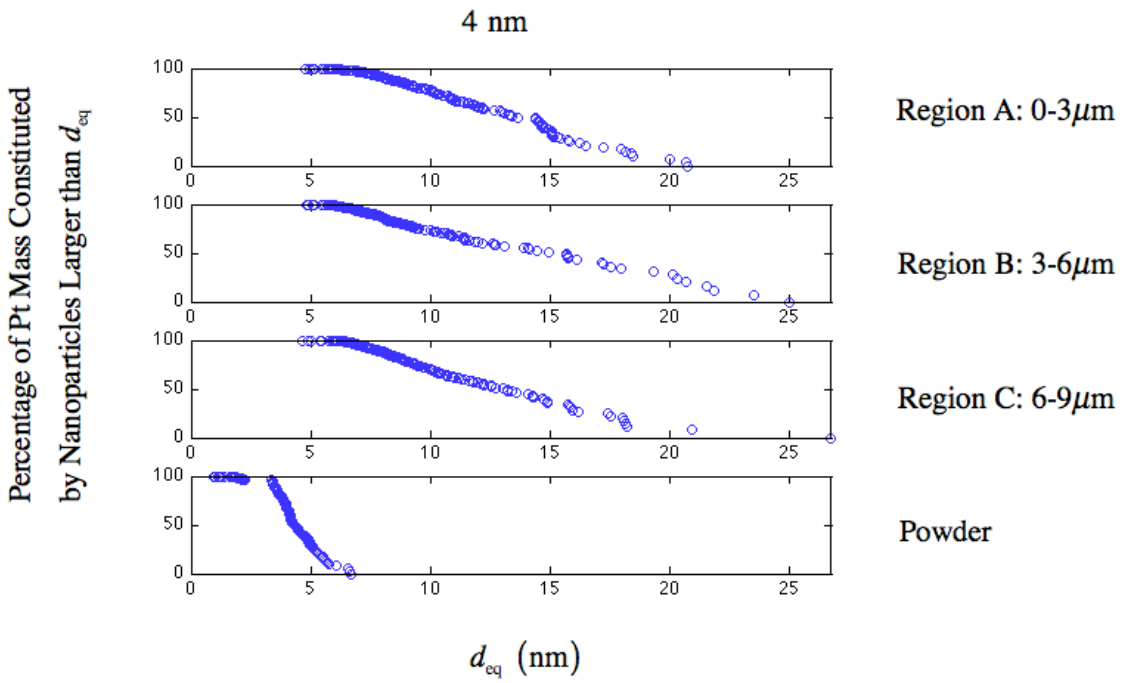

Figure 4.9: Mass percentage distributions for the 4 nm samples before and after cycling.

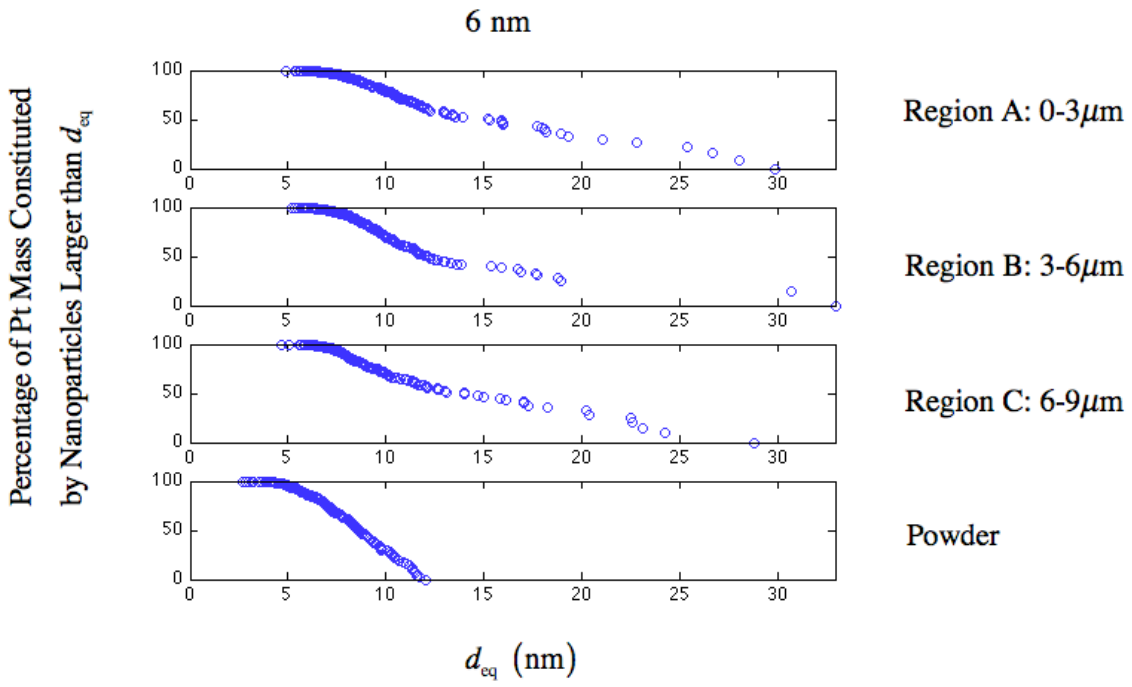

Figure 4.10: Mass percentage distributions for the 6 nm samples before and after cycling.

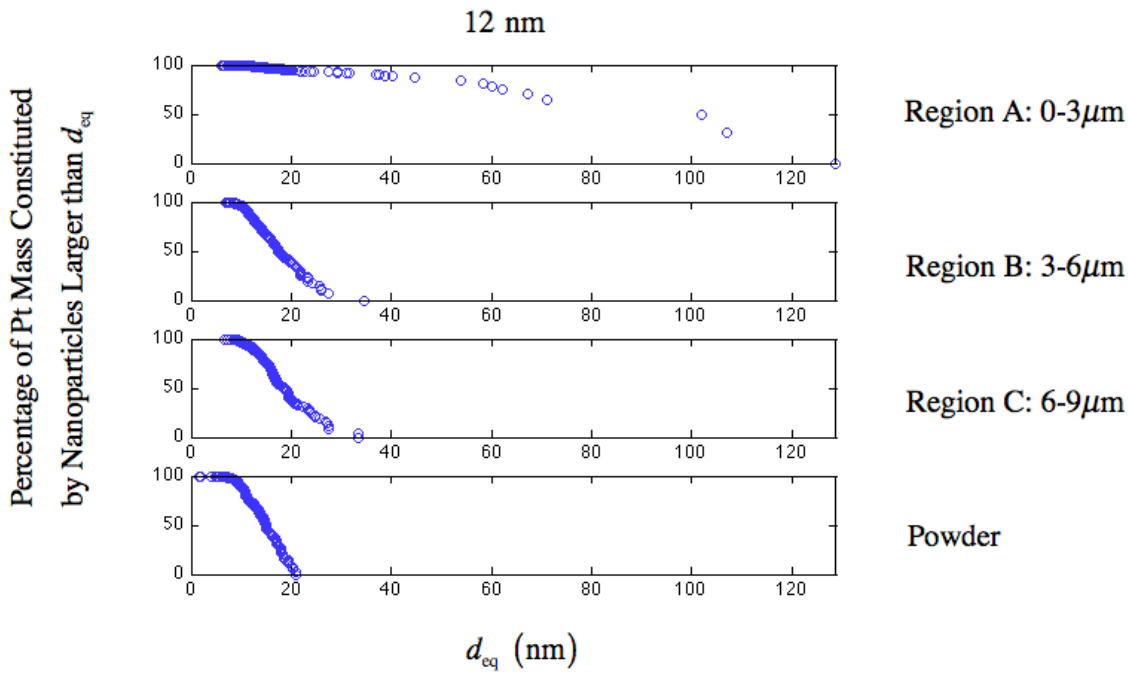

Figure 4.11: Mass percentage distributions for the 12 nm samples before and after cycling.

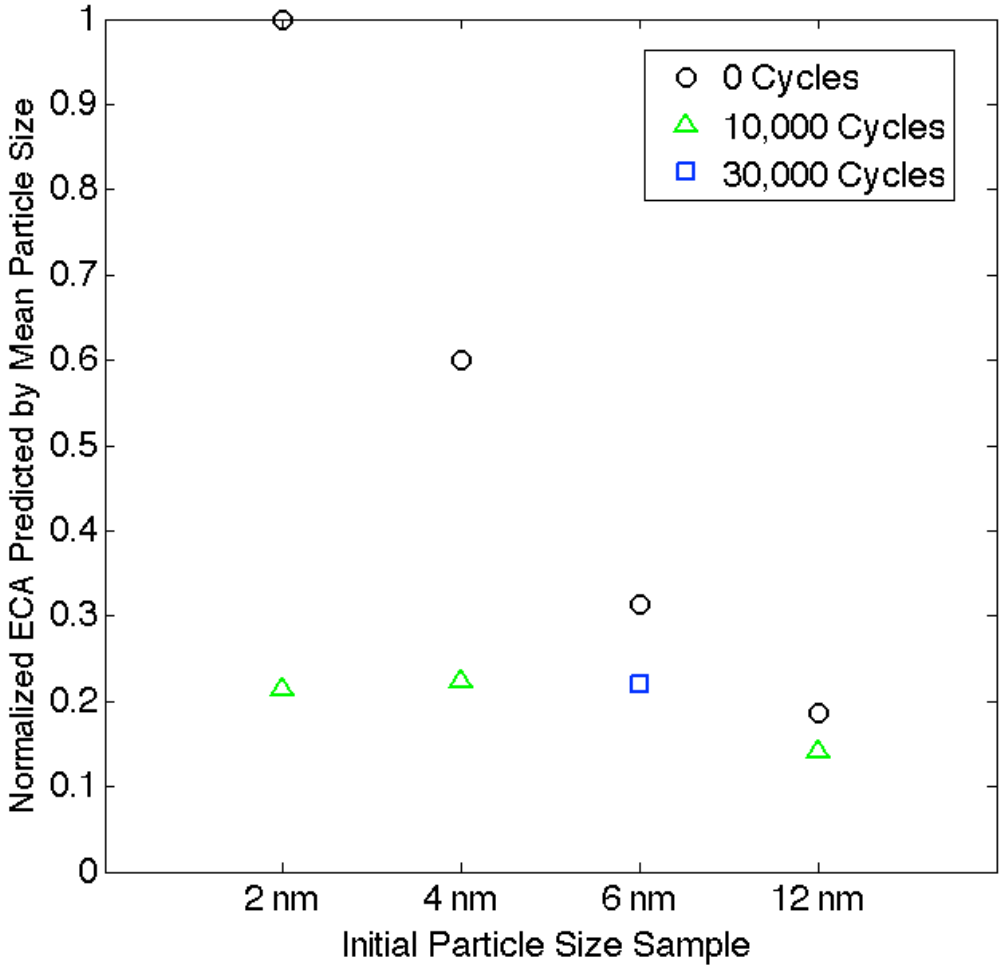

Figure 4.12: Comparisons of initial performance and durability across particle sizes.

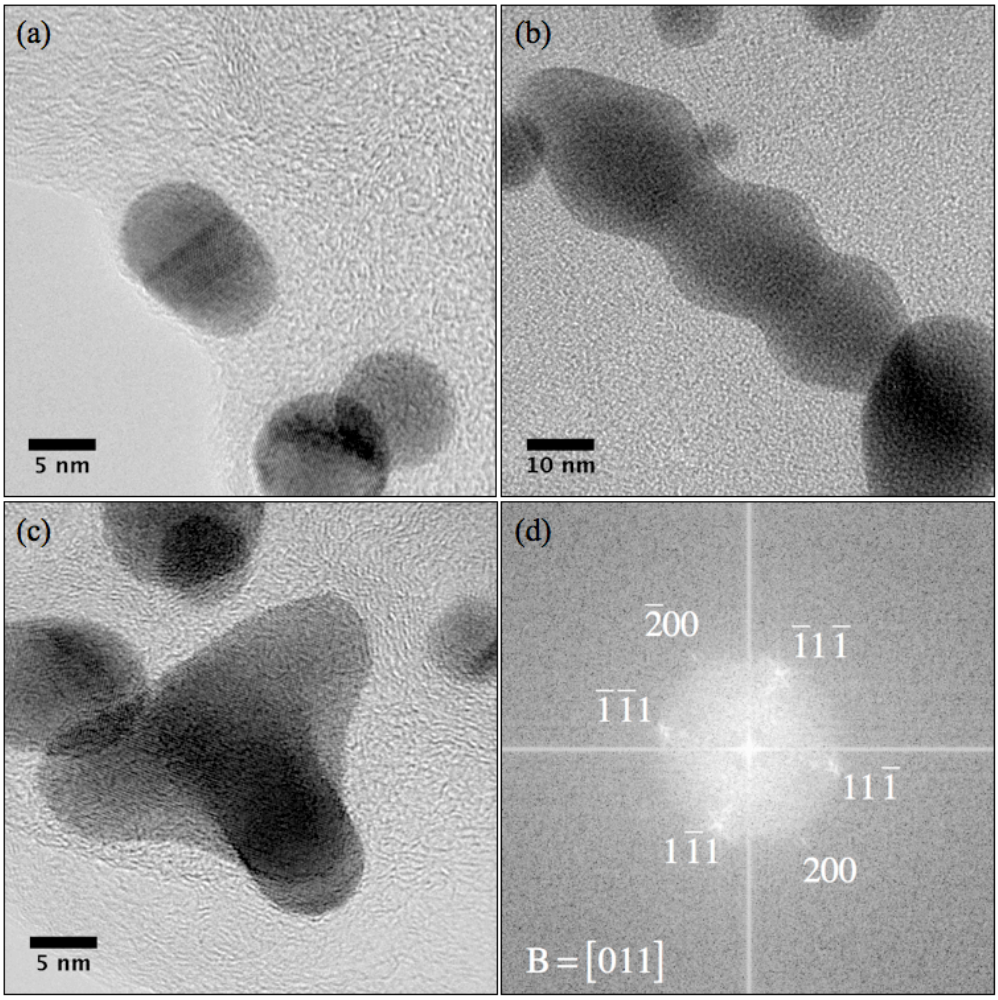

Figure 4.13: TEM characterization of coalesced and dendritic morphologies.

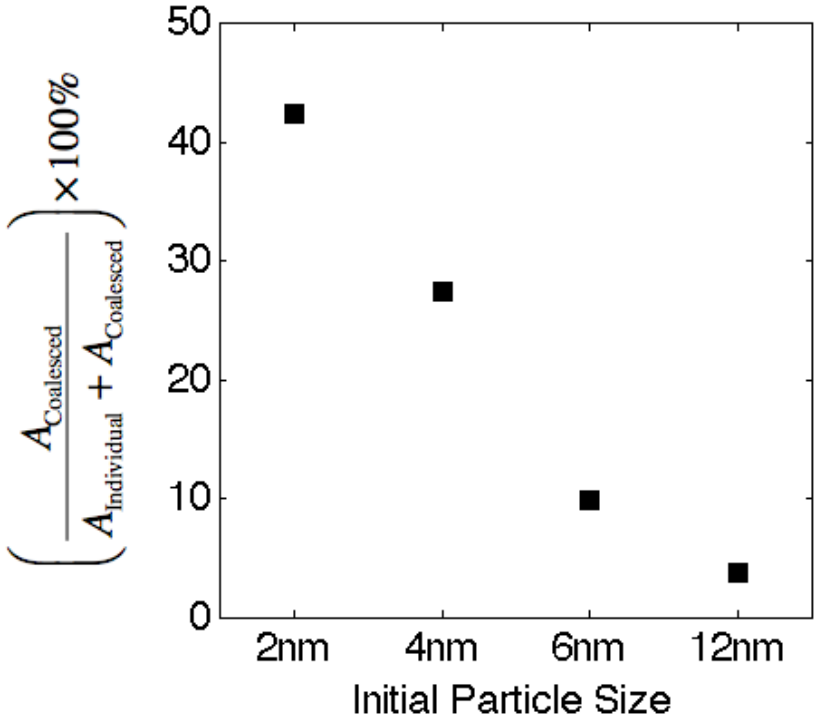

Figure 4.14: Area percentages of coalesced particles as a function of initial particle size.

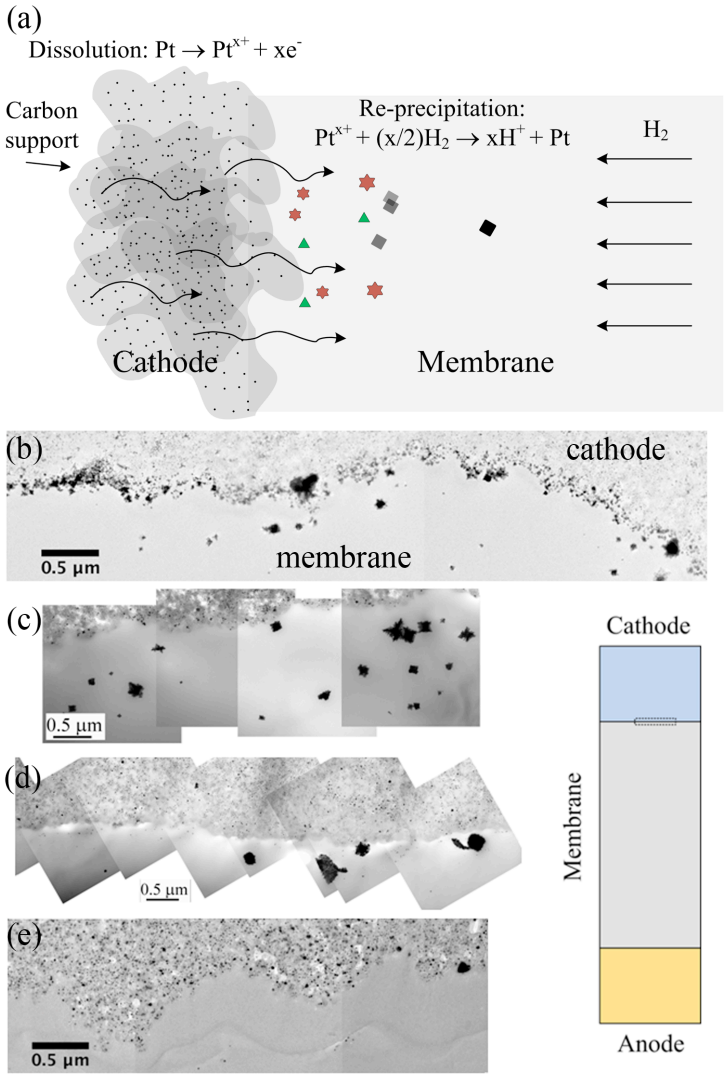

Figure 4.15: Pt bands at the cathode membrane interfaces formed by D&R.

Chapter 5: Conclusion

The work in this thesis improves the state of standardization in TEM for nanometrology. The metrology studies of this thesis inform the approach to studying the role of particle size in the cathode of the PEMFC.

This thesis quantifies the inherent error of common size metrics, demonstrating that the equivalent diameter provides the most reliable metric for TEM. This thesis demonstrates that employing common shape metrics as exclusion criteria introduces error and variability to characterizing PSDs. The novel Gamma shape metric presented in this study provides a reliable means to eliminate analyst bias by quantitatively excluding particles with projections that are not approximately circular. Particle overlap has been shown to lead to unavoidable error in the PSD, but the mathematical model and simulation package developed in this thesis provide a means to minimize error by identifying root causes of overlap mischaracterization. The novel equivalent error metric developed in this thesis provides a foundation for a standardized image acquisition protocol that minimizes error due to pixel resolution.

This thesis provides several key insights into the role of initial particle size in the cathode of the PEMFC. Particles smaller than 5 nm are inherently unstable in the cathode of the PEMFC because they are most prone to Pt dissolution. ECA loss results primarily from Pt particle growth, with loss of Pt mass to the membrane playing a secondary role. Pt particle growth results from a combination of modified electrochemical Ostwald ripening, particle migration and coalescence, and dissolution and reprecipitation. ECA loss due to loss of Pt mass to the cathode membrane interface shows an inverse proportionality with initial particle size. ECA loss due to agglomerate formation shows an inverse proportionality with initial particle size. An initial PSD characterized by a

mean particle size of 6.7 nm offers an ideal balance between initial performance and durability. The enhanced durability of this PSD is attributable to particles smaller than 5 nm accounting for less than 5% of Pt mass in the initial PSD.

Bibliography

[1] T. Theisen, 'Natural gas for power generation and the automotive market', in: W. Vielstich, A. Lamm, H. Gasteiger (Eds.), Handbook of Fuel Cells – Fundamentals, Technology and Applications, Vol. 3, John Wiley, Chichester, UK, 2003, pp. 25-38.

[2] T. M. I. Mahlia, R. Saidur, L. A. Memon, N. W. M. Zulkifli, H. H. Masjuki, Renew. Sust. Ener. Rev. 2010, 14, 3092-3099.

[3] H. A. Gasteiger, S. S. Kocha, B. Sompalli, F. T. Wagner, Appl. Catal. B 2005, 56, 9-35.

[4] F. Preli, Fuel Cells 2002, 2, 5-9.

[5] Y. Wang, K. S. Chen, J. Mishler, S. C. Cho, X. C. Adroher, Appl. Energy 2011, 88, 981-1007.

[6] M. F. Mathias, R. Makharia, H. A. Gasteiger, J. J. Conley, T. J. Fuller, C. J. Gittleman, S., S. Kocha, D. P. Miller, C. K. Mittelsteadt, T. Xie, S. G. Yan, P. T. Yu: "Two Fuel Cell Cars In Every Garage?", Interface 14 (2005) 24-35.

[7] M. Mathias, H. Gasteiger, R. Makharia, S. Kocha, T. Fuller, T. Xie, J. Pisco. "Can Available Membranes and Catalysts Meet Automotive Polymer Electrolyte Fuel Cell Requirements?" in A.C. Society (Ed.), American Chemical Society Fall National Meeting, Philadelphia, PA, 2004.

[8] F. A. de Bruijn, V. A. T. Dam, G. J. M. Janssen: "Durability and degradation issues of PEM fuel cell components", Fuel Cells 8 (2008) 3-22.

[9] J. Xie, D. L. Wood, K. L. More, P. Atanassov, R. L. Borup: "Microstructural changes of membrane electrode assemblies during PEFC durability testing at high humidity conditions", Journal of the Electrochemical Society 152 (2005) A1011-A20.

[10] M. W. Fowler, R. F. Mann, J. C. Amphlett, B. A. Peppley, P. R. Roberge: "Incorporation of voltage degradation into a generalised steady state electrochemical model for a PEM fuel cell", Journal of Power Sources 106 (2002) 274-83.

[11] M. S. Wilson, F. H. Garzon, K. E. Sickafus, S. Gottesfeld: "Surface-Area Loss of Supported Platinum in Polymer Electrolyte Fuel-Cells", Journal of the Electrochemical Society 140 (1993) 2872-77.

[12] T. Tada, T. Kikinzoku, in W. Vielstich, H.A. Gasteiger, A. Lamm (Eds.), Handbook of fuel cells - fundamentals, technology and applications. John Wiley and Sons, 2003, p. 481.

[13] J. Xie, D. L. Wood, D. M. Wayne, T. A. Zawodzinski, P. Atanassov, R. L. Borup: "Durability of PEFCs at high humidity conditions", Journal of the Electrochemical Society 152 (2005) A104-A13.

[14] T. Akita, A. Taniguchi, J. Maekawa, Z. Sirorna, K. Tanaka, M. Kohyama, K. Yasuda: "Analytical TEM study of Pt particle deposition in the proton-exchange membrane of a membrane-electrode-assembly", Journal of Power Sources 159 (2006) 461-67.

[15] Y. Shao-Horn, W. C. Sheng, S. Chen, P. J. Ferreira, E. F. Holby, D. Morgan: "Instability of supported platinum nanoparticles in low-temperature fuel cells", Topics in Catalysis 46 (2007) 285-305.

[16] K. Yasuda, A. Taniguchi, T. Akita, T. Ioroi, Z. Siroma: "Platinum dissolution and deposition in the polymer electrolyte membrane of a PEM fuel cell as studied by potential cycling", Physical Chemistry Chemical Physics 8 (2006) 746-52.

[17] R. L. Borup, J. R. Davey, F. H. Garzon, D. L. Wood, M. A. Inbody: "PEM fuel cell electrocatalyst durability measurements", Journal of Power Sources 163 (2006) 76-81.

[18] T. Patterson, Fuel Cell Technology: Opportunities and Challenges, Topical Conference Proceedings, AIChE Spring National Meeting, New York, 2002, p. 313-18.

[19] M. C. Smith, J. A. Gilbert, J. R. Mawdsley, S. Seifert, D. J. Myers: "In situ small-angle Xray scattering observation of Pt catalyst particle growth during potential cycling", Journal of the American Chemical Society 130 (2008) 8112-13.

[20] M. S. Wilson, F. H. Garzon, K. E. Sickafus, S. Gottesfeld, J. Electrochem. Soc. 1993, 140, 2872-2877.

[21] R. M. Darling, J. P. Meyers, J. Electrochem. Soc. 2003, 150, A1523-A1527.

[22] R. M. Darling, J. P. Meyers, J. Electrochem. Soc. 2005, 152, A242-A247.

[23] J. Xie, D. L. Wood III, K. L. More, P. Atanassov, R. L. Borup, J. Electrochem. Soc. 2005, 152, A104-A113.

[24] J. Xie, D. L. Wood III, D. M. Wayne, T. A. Zawodzinski, P. Atanassov, R. L. Borup, J. Electrochem. Soc. 2005, 152, A1011-A1020.

[25] R. L. Borup, J. R. Davey, F. H. Garzon, D. L. Wood, M. A. Inbody, J. Power Sources 2006, 163, 76-81.

[26] D. Ozkaya, Platinum Metals Review, 52(1), 61–62, (2008).

[27] P. J. Ferreira, G. J. La O, Y. Shao-Horn, D. Morgan, R. Makharia, S. Kocha, H. A. Gastaeiger, J. Electrochem. Soc. 2005, 152, A2256-A2271.

[28] P. J. Ferreira, Y. Shao-Horn, Electrochem. Solid-state Lett. 2007, 10, B60-B63.

[29] E. Guilminot, A. Corcella, F. Charlot, F. Maillard, M. Chatenet, J. Electrochem. Soc. 2007, 154, B96-B105.

[30] E. F. Holby, W. Sheng, Y. S-Horn, D. Morgan, Energy Environ. Sci. 2009, 2, 865-871.

[31] K. Hartl, M. Hanslik, M. Arenz, Energy Environ. Sci. 2011, 4, 234-238.

[32] T. Madden, D. Weiss, N. Cipollini, D. Condit, M. Gummalla, S. Burlatsky, V. Atrazhev, J. Electrochem. Soc. 2009, 156, B657-B662.

[33] M. Gummalla, V. V. Atrazhev, D. Condit, N. Cipollini, T. Madden, N. Y. Kuzminyh, D. Weiss, S. F. Burlatsky, J. Electrochem. Soc. 2010, 157, B1542-B1548.

[34] K. H. Kangasniemi, D. A. Condit, T. D. Jarvi, J. Electrochem. Soc. 2004, 151, E125-E132

[35] M. Cai, M. S. Ruthkosky, B. Merzougui, S. Swathirajan, M. P. Balogh, S. H. Oh, J. Power Sources 2006, 160, 977-986.

[36] S. C. Ball, S. L. Hudson, D. Thompsett, B. Theobald, J. Power Sources 2007, 171, 18-25.

[37] R. Makharia, S. Kocha, P. T. Yu, M. A. Sweikart, W. Gu, F. T. Wagner, H. A. Gasteiger: "Durable PEM Fuel Cell Electrode Materials: Requirements and Benchmarking Methodologies", ECS Transactions 1 (2006) 3-18.

[38] Z. Siroma, K. Ishii, K. Yasuda, Y. Miyazaki, M. Inaba, A. Tasaka: "Imaging of highly oriented pyrolytic graphite corrosion accelerated by Pt particles", Electrochemistry Communications 7 (2005) 1153-56.

[39] C. C. Granqvist, R. A. Buhrman: "Size Distributions for Supported Metal-Catalysts - Coalescence Growth Versus Ostwald Ripening", Journal of Catalysis 42 (1976) 477-79.

[40] Chen J., Chan K.Y. (2005) Mol Simul 31:527

[41] Bett J.A., Kinoshita K., Stonehart P. (1974) J Catal 35:307

[42] Lopez, N., T.V.W. Janssens, B.S. Clausen, Y. Xu, M. Mavrikakis, T. Bligaard, J.K. Nørskov, J. Catal. 223 (2004) 232.

[43] Buttrey, D; Pyrz, W; Langmuir. 2008, 24, 11350-11360

[44] Gontard, L.C; Ozkaya, D; Dunin-Borkowski, R.E.; Ultramicroscopy. 2011, 111, 101–106.

[45] Nanometrology. Eighth Nanoforum Report, Spring 2006. http://www.nanoforum.org

[46] Merkus, H.G. Particle Size Measurements. Springer Netherlands, 2008.

[47] Weisstein, Eric W. "Truncated Octahedron." From MathWorld--A Wolfram Web Resource. http://mathworld.wolfram.com/TruncatedOctahedron.html